
Doctoral Dissertations

Student Theses and Dissertations

Spring 2013

Numerical modeling of heat transfer and fluid flow in laser metal deposition by powder injection

Zhiqiang Fan

Follow this and additional works at: https://scholarsmine.mst.edu/doctoral_dissertations



Part of the [Mechanical Engineering Commons](#)

Department: Mechanical and Aerospace Engineering

Recommended Citation

Fan, Zhiqiang, "Numerical modeling of heat transfer and fluid flow in laser metal deposition by powder injection" (2013). *Doctoral Dissertations*. 2227.

https://scholarsmine.mst.edu/doctoral_dissertations/2227

This thesis is brought to you by Scholars' Mine, a service of the Missouri S&T Library and Learning Resources. This work is protected by U. S. Copyright Law. Unauthorized use including reproduction for redistribution requires the permission of the copyright holder. For more information, please contact scholarsmine@mst.edu.

NUMERICAL MODELING OF HEAT TRANSFER AND FLUID FLOW
IN LASER METAL DEPOSITION BY POWDER INJECTION

by

ZHIQIANG FAN

A DISSERTATION

Presented to the Faculty of the Graduate School of the
MISSOURI UNIVERSITY OF SCIENCE AND TECHNOLOGY

In Partial Fulfillment of the Requirements for the Degree

DOCTOR OF PHILOSOPHY

in

MECHANICAL ENGINEERING

2013

Approved

Dr. Frank Liou, Advisor

Dr. Joseph W. Newkirk

Dr. K. Chandrashekhara

Dr. Kelly Homan

Dr. Xiaoping Du

© 2013
Zhiqiang Fan
All Rights Reserved

PUBLICATION DISSERTATION OPTION

This dissertation consists of the following three articles that have been published, submitted for publication, or will be submitted for publication as follows:

Pages 3 – 42 were published in *Titanium Alloys - Towards Achieving Enhanced Properties for Diversified Applications* (book edited by A.K.M. Nurul Amin, ISBN 978-953-51-0354-7).

Pages 43 – 69 are intended for submission to *Applied Mathematical Modelling*.

Pages 70 – 101 are intended for submission to *Applied Mathematical Modelling*.

ABSTRACT

Laser metal deposition is an additive manufacturing technique which allows quick fabrication of fully-dense metallic components directly from Computer Aided Design (CAD) solid models. A self-consistent three-dimensional model was developed for the laser metal deposition process by powder injection, which simulates heat transfer, phase changes, and fluid flow in the melt pool. The governing equations for solid, liquid and gas phases in the calculation domain have been formulated using the continuum model. The free surface in the melt pool has been tracked by the Volume of Fluid (VOF) method, while the VOF transport equation was solved using the Piecewise Linear Interface Calculation (PLIC) method. Surface tension was modeled by taking the Continuum Surface Force (CSF) model combined with a force-balance flow algorithm. Laser-powder interaction was modeled to account for the effects of laser power attenuation and powder temperature rise during the laser metal deposition process.

The governing equations were discretized in the physical space using the finite volume method. The advection terms were approximated using the MUSCL flux limiter scheme. The fluid flow and energy equations were solved in a coupled manner. The incompressible flow equations were solved using a two-step projection method, which requires a solution of a Poisson equation for the pressure field. The discretized pressure Poisson equation was solved using the ICCG (Incomplete Cholesky Conjugate Gradient) solution technique. The energy equation was solved by an enthalpy-based method. Temperature-dependent thermal-physical material properties were considered in the numerical implementation. The numerical model was validated by comparing simulations with experimental measurements.

ACKNOWLEDGMENTS

I would like to express my sincere gratitude to Dr. Frank Liou, my graduate advisor, for his idea, direction and encouragement during my graduate study at Missouri S&T. I am also very grateful for his generous financial support for my study.

I would like to thank Dr. Joseph Newkirk for his advice and help in my research. His direction in my graduate work was invaluable and will be forever appreciated.

I would also like to thank my doctoral committee members, Dr. K. Chandrashekhara, Dr. Kelly Homan and Dr. Xiaoping Du, for serving on my dissertation examination committee and the various ways in which they assisted me in my study.

I would like to thank all members in LAMP lab, Todd, Jianzhong, Tian, Xueyang, Heng, and Praneeth, for making my research and study at Missouri S&T valuable and memorable. I would like to thank Rodney for his help with my research. I would also like to give my thanks to department secretaries, Gail Richards, Kathy Wagner and Lila Kolker, who helped and provided timely information.

This research was supported by US National Aeronautics and Space Administration (NASA) Grant Number NNX11AI73A, Product Innovation and Engineering, LLC, Army Research Office, Air Force Research Laboratory and Missouri S&T's Intelligent Systems Center, Manufacturing Engineering program and Material Research Center. Their support is appreciated.

Finally, I would like to thank my family, especially my parents and my wife, Yongqing Jiang, for their untiring support and encouragement, which took shape in so many ways. I thank my kids, Eric and Charles, for the vitality they brought to my life. Love from family was and will always be strength to me.

TABLE OF CONTENTS

	Page
PUBLICATION DISSERTATION OPTION	iii
ABSTRACT	iv
ACKNOWLEDGMENTS	v
LIST OF ILLUSTRATIONS	ix
LIST OF TABLES	xi
SECTION.....	1
1. INTRODUCTION	1
PAPER	3
I. NUMERICAL MODELING OF LASER DEPOSITION IN TITANIUM ALLOYS	3
1. INTRODUCTION	3
1.1. Additive Manufacturing.	4
1.2. Modeling of Melting/Solidification Phase Change	6
1.3. Modeling of Free-surface Flow	8
2. MATHEMATICAL MODEL	10
2.1. Governing Equations.	10
2.2. Surface Tension.	14
2.3. Tracking of the Free Surface.	16
2.4. Boundary Conditions.....	17
2.5. Numerical Implementation.....	18
3. SIMULATION RESULTS AND MODEL VALIDATION.....	21
4. CONCLUSIONS.....	30

5. ACKNOWLEDGEMENTS	33
6. REFERENCES	33
II. NUMERICAL AND ANALYTICAL MODELING OF LASER DEPOSITION WITH PREHEATING	43
ABSTRACT.....	43
1. INTRODUCTION	43
2. NUMERICAL MODEL	46
2.1. Governing Equations.....	46
2.2. Tracking of the Solid/Liquid Interface.....	49
2.3. Tracking of the Free Surface	49
2.4. Formulation of Source Term.....	50
2.5. Boundary Conditions.....	51
2.6. Numerical Algorithm	53
3. ANALYTICAL MODEL.....	54
3.1. Solution of a Disc Heat Source with a Uniform Intensity Distribution, Moving on the Surface of a Semi-infinite Medium	54
3.2. Solution of a Disc Heat Source with a Uniform Intensity Distribution, Considering the Boundary Conditions of the Bottom and Side Surfaces	55
3.3. Temperature Consideration for Thermo-Physical Properties.....	56
4. NUMERICAL SIMULATION AND EXPERIMENTS.....	58
4.1. Numerical Simulation.....	58
4.2. Experiments.....	58
4.3. Comparisons and Discussions	62
5. CONCLUSIONS.....	67

6. ACKNOWLEDGEMENTS	68
7. REFERENCES	68
III. THREE-DIMENSIONAL MODELING OF HEAT TRANSFER AND FLUID FLOW IN LASER METAL DEPOSITION BY POWER INJECTION	70
ABSTRACT.....	70
1. INTRODUCTION	70
2. MATHEMATICAL FORMULATION	74
2.1. Governing Equations.....	74
2.2. Free Surface Tracking	79
2.3. Surface Tension.....	80
2.4. Laser-Powder Interaction	83
2.5. Boundary Conditions.....	85
2.6. Numerical Implementation.....	88
3. RESULTS AND DISCUSSION	91
4. CONCLUSIONS.....	96
5. ACKNOWLEDGEMENTS	97
6. REFERENCES	97
SECTION	
2. CONCLUSIONS.....	102
VITA	104

LIST OF ILLUSTRATIONS

Figure	Page
PAPER I	
1. Schematics of a Coaxial Laser Metal Deposition System with Powder Injection.....	6
2. Schematic Diagram of the Calculation Domain for Laser Metal Deposition Process..	11
3. Simulation Results of Laser Deposition of Ti-6Al-4V	23
4. Schematic of Experimental Setup.....	25
5. Melt Pool Peak Temperature Comparison between Simulation and Experiment at Different Laser Power Levels	25
6. Melt Pool Peak Temperature Comparison between Simulation and Experiment at Different Travel Speeds	26
7. Melt Pool Length Comparisons between Simulation and Experiment at Different Power Levels.....	26
8. Comparison of Dilution Depth between Simulation and Experiment at Different Power Levels.....	27
9. Comparison of Dilution Depth between Simulation and Experiment at Different Travel Speeds and Different Laser Power	28
10. Comparison of Dilution Depth between Simulation and Experiment at Different Powder Mass Flow Rates and Different Laser Power Levels.....	28
11. Ultrasonic Graphs of a Laser Deposited Ti-6Al-4V Specimen	31
PAPER II	
1. Schematic of a Typical Laser Deposition System	44
2. Schematic of the Calculation Domain	47
3. Thermal Conductivity and Specific Heat as a Function of Temperature for Ti-6Al-4V [13].....	57
4. Simulation Results at $t = 225$ ms	60
5. Schematic of Experimental Setup.....	61

6. Comparisons between Experimental Measurements and Model Predictions at a Constant Powder Mass Flow Rate and a Constant Laser Scanning Speed.....	63
7. Comparisons between Experimental Measurements and Model Predictions at a Constant Powder Mass Flow Rate and a Constant Laser Power	64
8. Dilution Depth as a Function of Laser Power.....	66
9. Dilution Depth as a Function of Laser Travel Speed.....	66
10. Dilution Depth as a Function of Powder Mass Flow Rate.....	67

PAPER III

1. Schematics of a Coaxial Laser Metal Deposition System by Powder Injection.....	72
2. Schematic Diagram of the Calculation Domain for a Laser Deposition Process by Powder Injection	75
3. CSF Representation of a Liquid/Gas Interface	81
4. 3D Deposition Profile and Temperature Distribution with Cross Section at $t = 0.11$ s.....	93
5. Fluid Velocity Fields in the Melt Pool in Cross Section along the Laser Scanning Direction at $t = 0.11$ s.....	93
6. Comparison between Experimental and Calculated Deposit Width (a) and Deposit Height (b) at Different Laser Powers.....	94
7. Comparison between Experimental and Calculated Deposit Width (a) and Deposit Height (b) at Different Powder Mass Flow Rates.....	95

LIST OF TABLES

Table	Page
PAPER I	
1. Material Properties for Ti-6Al-4V and Main Process Parameters.....	20
PAPER II	
1. Distances and Their Projections.....	56
2. Material Properties for Ti-6Al-4V and Main Process Parameters.....	59
PAPER III	
1. Main Material Properties for Powder and Substrate.....	92

SECTION

1. INTRODUCTION

Laser metal deposition is an additive manufacturing technique which allows quick fabrication of fully-dense metallic components directly from Computer Aided Design (CAD) solid models. The applications include rapid prototyping, rapid tooling and part refurbishment. Laser metal deposition has an important advantage for these applications because it can produce near-net shape parts with little or no machining. Laser deposition uses a focused laser beam as a heat source to create a melt pool on an underlying substrate. Powder material is then injected into the melt pool through nozzles. The incoming powder is metallurgically bonded with the substrate upon solidification. The part is fabricated in a layer by layer manner in a shape that is dictated by the CAD solid model. Laser metal deposition is characterized by small melt pool size, rapid changes of temperature and very short duration of the process. These characteristics make physical measurements of important parameters such as temperature and velocity fields, solidification rate and thermal cycles during laser metal deposition very difficult. These parameters are important because the melt pool convection patterns and the heating and cooling rates determine the geometry, composition, structure and the resulting properties of the deposit. For example, the buoyancy-driven flow due to temperature and species gradients in the melt pool strongly influences the microstructure and thus the mechanical properties of the final products. The surface tension-driven free-surface flow determines the shape and smoothness of the deposit. Numerical simulations can give reasonable estimates of these parameters.

Laser metal deposition involves many process parameters, including total power and power intensity distribution of the energy source, travel speed, translation path, material feed rate and shielding gas pressure. Physical phenomena associated with laser deposition processes are complex, including melting/solidification and vaporization phase changes, free-surface flow with surface tension, heat and mass transfer, and moving heat source, and laser metal interaction. The variable process parameters together with the interacting physical phenomena involved in AM complicate the development of process-property relationships and appropriate process control. Thus, an effective numerical modelling of the processing is very useful for assessing the impact of process parameters and predicting optimized conditions.

PAPER

I. NUMERICAL MODELING OF LASER DEPOSITION IN TITANIUM ALLOYS

1. INTRODUCTION

It is easy to understand why industry and, especially, aerospace engineers love titanium. Titanium parts weigh roughly half as much as steel parts, but its strength is far greater than the strength of many alloy steels giving it a very high strength-to-weight ratio. Most titanium alloys are poor thermal conductors, thus heat generated during cutting does not dissipate through the part and machine structure, but concentrates in the cutting area. The high temperature generated during the cutting process also causes a work hardening phenomenon that affects the surface integrity of titanium, and could lead to geometric inaccuracies in the part and severe reduction in its fatigue strength [Benes, 2007]. On the contrary, additive manufacturing (AM) is an effective way to process titanium alloys as AM is principally thermal based, the effectiveness of AM processes depends on the material's thermal properties and its absorption of laser energy rather than on its mechanical properties. Therefore, brittle and hard materials can be processed easily if their thermal properties (e.g., conductivity, heat of fusion, etc.) are favourable, such as titanium. Cost effectiveness is also an important consideration for using additive manufacturing for titanium processing. Parts or products cast and/or machined from titanium and its alloys are very expensive, due to the processing difficulties and

complexities during machining and casting. AM processes however, have been found to be very cost effective because they can produce near-net shape parts from these high performance metals with little or no machining [Liou & Kinsella, 2009]. In the aerospace industry, titanium and its alloys are used for many large structural components. When traditional machining/cast routines are adopted, conversion costs for these heavy section components can be prohibitive due to long lead time and low-yield material utilization [Eylon & Froes, 1984]. AM processes have the potential to shorten lead time and increase material utilization in these applications. The following Sections 1.1, 1.2 and 1.3 summarize the fundamental knowledge for the modeling of additive manufacturing processes.

1.1. Additive Manufacturing. Additive manufacturing can be achieved by powder based spray (e.g., thermal spray or cold spray), sintering (e.g., selective laser sintering), or fusion-based processes (or direct metal deposition) which use a laser beam, an electron beam, a plasma beam, or an electric arc as an energy source and either metallic powder or wire as feedstock [Kobryn et al., 2006]. For the aerospace industry which is the biggest titanium market in the U.S. [Yu & Imam, 2007], fusion-based AM processes are more advantageous since they can produce 100% dense functional metal parts. This chapter will focus on fusion-based AM processes with application to titanium. Numerical modeling and simulation is a very useful tool for assessing the impact of process parameters and predicting optimized conditions in AM processes. AM processes involve many process parameters, including total power and power intensity distribution of the energy source, travel speed, translation path, material feed rate and shielding gas pressure. These process parameters not only vary from part to part, but also frequently

vary locally within a single part to attain the desired deposit shape [Kobryn et al., 2006]. Physical phenomena associated with AM processes are complex, including melting/solidification and vaporization phase changes, surface tension-dominated free-surface flow, heat and mass transfer, and moving heat source. The variable process parameters together with the interacting physical phenomena involved in AM complicate the development of process-property relationships and appropriate process control. Thus, an effective numerical modeling of the processing is very useful for assessing the impact of process parameters and predicting optimized conditions.

Currently, process-scale modeling mainly addresses transport phenomena such as heat transfer and fluid dynamics, which are closely related to the mechanical properties of the final structure. For example, the buoyancy-driven flow due to temperature and species gradients in the melt pool strongly influences the microstructure and thus the mechanical properties of the final products. The surface tension-driven free-surface flow determines the shape and smoothness of the clad. In this chapter, numerical modeling of transport phenomena in fusion-based AM processes will be presented, using the laser metal deposition process as an example. Coaxial laser deposition systems with blown powder as shown in Figure 1 are considered for simulations and experiments. The material studied is Ti-6Al-4V for both the substrate and powder. As the main challenges in modeling of fusion-based AM processes are related to melting/solidification phase change and free-surface flow in the melt pool, modeling approaches for these physical phenomena will be introduced in Sections 1.2 and 1.3.

1.2. Modeling of Melting/Solidification Phase Change. Fusion-based AM processes involve a melting/solidification phase change. Numerical modeling of the solidification of metal alloys is very challenging because a general solidification of metal alloys involves a so-called “mushy region” over which both solid and liquid coexist and the transport phenomena occur across a wide range of time and length scales [Voller, 2006].

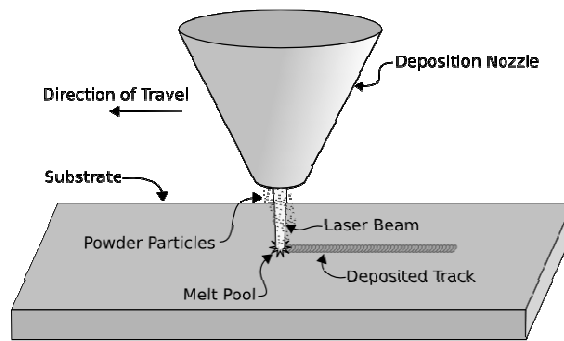


Figure 1. Schematics of a Coaxial Laser Metal Deposition System with Powder Injection

A rapidly developing approach that tries to resolve the smallest scales of the solid-liquid interface can be thought of as direct microstructure simulation. In order to simulate the microstructure development directly, the evolution of the interface between different phases or different microstructure constituents has to be calculated, coupled with the physical fields such as temperature and concentration [Pavlyk & Dilthey, 2004].

To this approach belong phase-field [Beckermann et al., 1999; Boettinger et al., 2002; Caginalp, 1989; Karma & Rappel, 1996,1998; Kobayashi,1993; Provatas et al., 1998; Steinbach et al., 1996; Warren & Boettinger, 1995; Wheeler et al., 1992], cellular-automaton [Boettinger et al., 2000; Fan et al., 2007a; Gandin & Rappaz, 1994; Grujicic et al. 2001; Rappaz & Gandin, 1993; Zhu et al., 2004], front tracking [Juric & Tryggvason, 1996; Sullivan et al., 1987; Tryggvason et al., 2001], immersed boundary [Udaykumar et al., 1999, 2003] and level set [Gibou et al., 2003; Kim et al. 2000] methods. Due to the limits of current computing power, the above methods only apply to small domains on a continuum scale from about 0.1 μm to 10 mm.

To treat the effects of transport phenomena at the process-scale ($\sim 1\text{ m}$), a macroscopic model needs to be adopted, where a representative volume element (REV) is selected to include a representative and uniform sampling of the mushy region such that local scale solidification processes can be described by variables averaged over the REV [Voller et al., 2004]. Based on the REV concept, governing equations for the mass, momentum, energy and species conservation at the process scale are developed and solved. Two main approaches have been used for the derivation and solution of the macroscopic conservation equations. One approach is the two-phase model [Beckermann & Viskanta, 1988; Ganesan & Poirier, 1990; Ni & Beckermann, 1991], in which the two phases are treated as separate and separate volume-averaged conservation equations are derived for solid and liquid phases using a volume averaging technique. This approach gives the complete mathematical models for solidification developed today, which have the potential to build a strong linkage between physical phenomena occurring on macroscopic and microscopic scales [Ni & Incropera, 1995]. However, the numerical

procedures of this model are fairly involved since two separate sets of conservation equations need to be solved and the interface between the two phases must be determined for each time step [Jaluria, 2006]. This places a great demand on computational capabilities. In addition, the lack of information about the microscopic configuration at the solid-liquid interface is still a serious obstacle in the implementation of this model for practical applications [Stefanescu, 2002]. An alternative approach to the development of macroscopic conservation equations is the continuum model [Bennon & Incropera, 1987; Hills et al., 1983; Prantil & Dawson, 1983; Prescott et al., 1991; Voller & Prakash, 1987; Voller et al., 1989]. This model uses the classical mixture theory [Muller, 1968] to develop a single set of mass, momentum, energy and species conservation equations, which concurrently apply to the solid, liquid and mushy regions. The numerical procedures for this model are much simpler since the same equations are employed over the entire computational domain, thereby facilitating use of standard, single-phase CFD procedures. In this study, the continuum model is adopted to develop the governing equations.

1.3. Modeling of Free-surface Flow. In fusion-based AM processes, the melt pool created by the energy source on the substrate is usually modelled as a free-surface flow, in which the pressure of the lighter fluid is not dependent on space, and viscous stresses in the lighter fluid is negligible. The techniques to find the shape of the free surface can be classified into two major groups: Lagrangian (or moving grid) methods and Eulerian (or fixed grid) methods. In Lagrangian methods [Hansbo, 2000; Idelsohn et al., 2001; Ramaswamy & Kahawara, 1987; Takizawa et al., 1992], every point of the liquid domain is moved with the liquid velocity. A continuous re-meshing of the domain or part of it is

required at each time step so as to follow the interface movement. A special procedure is needed to enforce volume conservation in the moving cells. All of this can lead to complex algorithms. They are mainly used if the deformation of the interface is small, for example, in fluid-structure interactions or small amplitude waves [Caboussat, 2005]. In Eulerian methods, the interface is moving within a fixed grid, and no re-meshing is needed. The interface is determined from a field variable, for example, a volume fraction [DeBar, 1974; Hirt & Nichols, 1981; Noh & Woodward, 1976], a level-set [Sethian, 1996, 1999] or a phase-field [Boettinger et al., 2002; Jacqmin, 1999]. While Lagrangian techniques are superior for small deformations of the interfaces, Eulerian techniques are usually preferred for highly distorted, complex interfaces, which is the case for fusion-based additive manufacturing processes. For example, in AM processes with metallic powder as feedstock, powder injection causes intermittent mergers and breakups at the interface of the melt pool, which needs a robust Eulerian technique to handle.

Among the Eulerian methods, VOF (for Volume-Of-Fluid) [Hirt & Nichols, 1981] is probably the most widely used. It has been adopted by many in-house codes and built into commercial codes (SOLA-VOF [Nichols et al, 1980], NASA-VOF2D [Torrey et al 1985], NASA-VOF3D [Torrey et al 1987], RIPPLE [Kothe & Mjolsness 1991], and FLOW3D [Hirt & Nichols 1988], ANSYS Fluent, to name a few). In this method a scalar indicator function, F , is defined on the grid to indicate the liquid-volume fraction in each computational cell. Volume fraction values between zero and unity indicate the presence of the interface. The VOF method consists of an interface reconstruction algorithm and a volume fraction advection scheme. The features of these two steps are used to distinguish different VOF versions. For modeling of AM processes, an advantage of VOF is that it

can be readily integrated with the techniques for simulation of the melting /solidification phase change. VOF methods have gone through a continuous process of development and improvement. Reviews of the historical development of VOF can be found in [Benson, 2002; Rider & Kothe, 1998; Rudman, 1997; Tang et al., 2004]. In earlier versions of VOF [Chorin, 1980; Debar, 1974; Hirt & Nichols, 1981; Noh & Woodward, 1976], reconstruction algorithms are based on a piecewise-constant or “stair-stepped” representation of the interface and advection schemes are at best first-order accurate. These first-order VOF methods are numerically unstable in the absence of surface tension, leading to the deterioration of the interface in the form of flotsam and jetsam [Scardovelli & Zaleski, 1999]. The current generation of VOF methods approximate the interface as a plane within a computational cell, and are commonly referred to as piecewise linear interface construction (PLIC) methods [Gueyffier et al., 1999; Rider & Kothe, 1998; Youngs, 1982, 1984]. PLIC-VOF is more accurate and avoids the numerical instability [Scardovelli & Zaleski, 1999].

2. MATHEMATICAL MODEL

2.1 Governing Equations. In this study, the calculation domain for a laser deposition system includes the substrate, melt pool, remelted zone, deposited layer and part of the gas region, as shown in Figure 2. The continuum model [Benetton & Incropera, 1987; Prescott et al., 1991] is adopted to derive the governing equations for melting and solidification with the mushy zone. Some important terms for the melt pool have been added in the momentum equations, including the buoyancy force term and surface

tension force term, while some minor terms in the original derivation in [Prescott et al., 1991] have been neglected. The molten metal is assumed to be Newtonian fluid, and the melt pool is assumed to be an incompressible, laminar flow. The laminar flow assumption can be relaxed if turbulence is considered by an appropriate turbulence model, such as a low-Reynolds-number k - ϵ model [Jones & Launder, 1973]. The solid and liquid phases in the mushy zone are assumed to be in local thermal equilibrium.

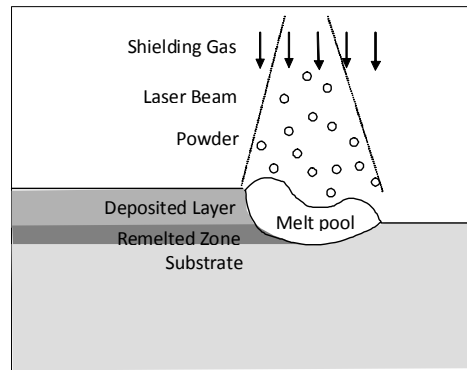


Figure 2. Schematic Diagram of the Calculation Domain
for Laser Metal Deposition Process

For the system of interest, the conservation equations are summarized as follows:

Mass conservation:

$$\frac{\partial \rho}{\partial t} + \nabla \cdot (\rho \mathbf{V}) = 0 \quad (1)$$

Momentum conservation:

$$\frac{\partial}{\partial t}(\rho u) + \nabla \cdot (\rho \mathbf{V}u) = \nabla \cdot \left(\mu_l \frac{\rho}{\rho_l} \nabla u \right) - \frac{\partial p}{\partial x} - \frac{\mu_l}{K_x} \frac{\rho}{\rho_l} (u - u_s) + \rho \mathbf{g}_x [1 - \alpha(T - T_0)] + \mathbf{F}_{sx} \quad (2)$$

$$\frac{\partial}{\partial t}(\rho v) + \nabla \cdot (\rho \mathbf{V}v) = \nabla \cdot \left(\mu_l \frac{\rho}{\rho_l} \nabla v \right) - \frac{\partial p}{\partial y} - \frac{\mu_l}{K_y} \frac{\rho}{\rho_l} (v - v_s) + \rho \mathbf{g}_y [1 - \alpha(T - T_0)] + \mathbf{F}_{sy} \quad (3)$$

Energy conservation:

$$\frac{\partial}{\partial t}(\rho h) + \nabla \cdot (\rho \mathbf{V}h) = \nabla \cdot (k \nabla T) - \nabla \cdot [\rho(h_l - h)(\mathbf{V} - \mathbf{V}_s)] + S \quad (4)$$

In equations (1)-(4), the subscripts s and l stand for solid and liquid phase, respectively. t , μ , and T are time, dynamic viscosity and temperature, respectively. u and v are x-direction and y-direction velocity components. The continuum density ρ , vector velocity \mathbf{V} , enthalpy h , and thermal conductivity k are defined as follows:

$$\rho = g_s \rho_s + g_l \rho_l \quad (5)$$

$$\mathbf{V} = f_s \mathbf{V}_s + f_l \mathbf{V}_l \quad (6)$$

$$h = f_s h_s + f_l h_l \quad (7)$$

$$k = g_s k_s + g_l k_l \quad (8)$$

Here, the subscripts s and l stand for solid and liquid phase, respectively. f_s and f_l refer to mass fractions of solid and liquid phases, and g_s and g_l are volume fractions of solid and liquid phases. To calculate these four quantities, a general practice is that g_l (or g_s) is calculated first and then the other three quantities are obtained according to the following relationships:

$$f_l = \frac{g_l \rho_l}{\rho} \quad f_s = \frac{g_s \rho_s}{\rho} \quad g_s + g_l = 1 \quad f_s + f_l = 1 \quad (9)$$

The volume fraction of liquid g_l can be found using different models, such as the level rule, the Scheil model [Scheil, 1942], or the Clyne and Kurz model [Clyne & Kurz, 1981]. For the target material Ti-6Al-4V, it is assumed that g_l is only dependent on temperature. The $g_l(T)$ function is given by [Swaminathan & Voller, 1992]:

$$g_l = \begin{cases} 0 & \text{if } T < T_s \\ \frac{T - T_s}{T_l - T_s} & \text{if } T_s \leq T \leq T_l \\ 1 & \text{if } T > T_l \end{cases} \quad (10)$$

The phase enthalpy for the solid and the liquid can be expressed as:

$$h_s = \int_0^T c_s(T) dT \quad (11)$$

$$h_l = \int_0^{T_s} c_s(T) dT + \int_{T_s}^T c_l(T) dT + L_m \quad (12)$$

where L_m is the latent heat of melting. c_s and c_l are specific heat of solid and liquid phases.

In equations (2) and (3), the third terms on the right-hand side are the drag interaction terms, and K_x and K_y are the permeability of the two-phase mushy zone in x- and y- directions, which can be calculated from various models [Bhat et al., 1995; Carman, 1937; Drummond & Tahir, 1984; Ganesan et al., 1992; Poirier, 1987; West, 1985]. Here the mushy zone is considered as rigid (i.e. a porous media). If the mushy zone is modeled as a slurry region, these two terms can be treated as in [Ni & Incropera, 1995]. In equations (2) and (3), the fourth terms on the right-hand side are the buoyancy force components due to temperature gradients. Here Boussinesq approximation is applied. α is the thermal expansion coefficient. The fifth terms on the right-hand side of equations (2) and (3) are surface tension force components, which will be described in Section 2.2 below. The term S in equation (4) is the heat source.

2.2. Surface Tension. The surface tension force, \mathbf{F}_S , is given by:

$$\mathbf{F}_S = \gamma\kappa\hat{\mathbf{n}} + \nabla_s\gamma \quad (13)$$

Where γ is surface tension coefficient, κ the curvature of the interface, $\hat{\mathbf{n}}$ the unit normal to the local surface, and ∇_s the surface gradient operator. The term $\gamma\kappa\hat{\mathbf{n}}$ is the normal component of the surface tension force. The term $\nabla_s\gamma$ represents the Marangoni effect caused by spatial variations in the surface tension coefficient along the interface due to temperature and/or species gradients. It causes the fluid flow from regions of lower to higher surface tension coefficient.

The conventional approach when dealing with surface tension is to use finite difference schemes to apply a pressure jump at a free-surface discontinuity. More recently, a general practice is to model surface tension as a volume force using a continuum model, either the Continuum Surface Force (CSF) model [Brackbill et al., 1992] or the Continuum Surface Stress (CSS) model [Lafaurie et al., 1994]. The volume force acts everywhere within a finite transition region between the two phases. In this study, the CSF model is adopted, which has been shown to make more accurate use of the free-surface VOF data [Brackbill et al., 1992].

A well-known problem with VOF (and other Eulerian methods) modeling of surface tension is so-called “parasitic currents” or “spurious currents”, which is a flow induced solely by the discretization and by a lack of convergence with mesh refinement. Under some circumstances, this artificial flow can be strong enough to dominate the solution, and the resulting strong vortices at the interface may lead to catastrophic instability of the interface and may even break-up [Fuster et al., 2009; Gerlach et al. 2006]. Two measures can be taken to relieve or even resolve this problem. One measure is to use a force-balance flow algorithm in which the CSF model is applied in a way that is consistent with the calculation of the pressure gradient field. Thus, imbalance between discrete surface tension and pressure-gradient terms can be avoided. Within a VOF framework, such force-balance flow algorithms can be found in [Francois et al., 2006; Y. Renardy & M. Renardy, 2002; Shirani et al., 2005]. In this study, the algorithm in [Shirani et al., 2005] is followed. The other measure is to get an accurate calculation of surface tension by accurately calculating interface normals and curvatures from volume fractions. For this purpose, many methods have been developed, such as those in

[Cummins et al, 2005; Francois et al., 2006; López & Hernández, 2010; Meier et al., 2002; Pilliod Jr. & Puckett, 2004; Y. Renardy & M. Renardy, 2002]. The method we use here is the height function (HF) technique, which has been shown to be second-order accurate, and superior to those based on kernel derivatives of volume fractions or RDF distributions [Cummins et al, 2005; Francois et al., 2006; Liovic et al., 2010].

Specifically, we adopt the HF technique in [López & Hernández, 2010] that has many improvements over earlier versions (such as that in [Torrey et al 1985]) of HF, including using an error correction procedure to minimize estimation error. Within the HF framework, suppose the absolute value of the y-direction component of the interface normal vector is larger than the x-direction component, interface curvature (in 2D) is given by

$$\kappa = \frac{H_{xx}}{(1 + H_x^2)^{3/2}} \quad (14)$$

where H is the height function, H_x and H_{xx} are first-order and second-order derivatives of H , respectively. H_x and H_{xx} are obtained by using a finite difference formula. Interface normals are also calculated based on the Least-Squares Fit method from [Aulisa et al., 2007].

2.3. Tracking of the Free Surface. The free surface of the melt pool is tracked using the PLIC-VOF [Gueyffier et al., 1999; Scardovelli & Zaleski, 2000, 2003]. The Volume of Fluid function, F , satisfies the following conservation equation:

$$\frac{\partial F}{\partial t} + (\mathbf{V} \cdot \nabla)F = 0 \quad (15)$$

The PLIC-VOF method consists of two steps: interface reconstruction and interface advection. In 2D calculation, a reconstructed planar surface becomes a straight line which satisfies the following equation:

$$n_x x + n_y y = d \quad (16)$$

where n_x and n_y are x and y components of the interface normal vector. d is a parameter related to the distance between the line and the coordinate origin of the reference cell. In the interface reconstruction step, n_x and n_y of each cell are calculated based on volume fraction data, using the Least-Squares Fit method from [Aulisa et al., 2007]. Then the parameter d is determined to match the given volume fraction. Finally given the velocity field, the reconstructed interface is advected according to the combined Eulerian-Lagrangian scheme in [Aulisa et al., 2007].

2.4. Boundary Conditions. Energy balance at the free surface satisfies the following equation:

$$k \frac{\partial T}{\partial \mathbf{n}} = \frac{\eta(P_{laser} - P_{atten})}{\pi R^2} - h_c(T - T_\infty) - \varepsilon\sigma(T^4 - T_\infty^4) - \dot{m}_e L_v \quad (17)$$

where terms on the right-hand side are laser irradiation, convective heat loss, radiation heat loss and evaporation heat loss, respectively. P_{laser} is the power of laser beam, P_{atten}

the power attenuated by the powder cloud, R the radius of laser beam spot, η the laser absorption coefficient, \dot{m}_e the evaporation mass flux, L_v the latent heat of evaporation, hc the heat convective coefficient, ε emissivity, σ the Stefan-Boltzmann constant, and \mathbf{n} the normal vector at the local interface. \dot{m}_e can be evaluated according to the “overall evaporation model” in [Choi et al., 1987], and P_{atten} can be calculated according to [Frenk et al., 1997] with a minor modification.

On the bottom surface and side surfaces, boundary conditions are given by Equations (18) – (19). Note that the radiation heat loss at these surfaces is neglected due to the fact that the temperature differences at these surfaces are not large.

$$k \frac{\partial T}{\partial \mathbf{n}} + h_c (T - T_\infty) = 0 \quad (18)$$

$$\mathbf{V} = 0 \quad (19)$$

2.5. Numerical Implementation. Finite difference and finite volume methods are used for spatial discretization of the governing equations. Staggered grids are employed where the temperatures, pressures and VOF function are located at the cell center and the velocities at the walls. In the numerical implementation, material properties play an important role. The material properties are generally dependent on temperature, concentration, and pressure. For fusion-based additive manufacturing processes, the material experiences a large variation from room temperature to above the melting temperature. For Ti-6Al-4V, many material properties experience large variations over

this wide temperature range, as shown in Table 1. For example, the value of specific heat varies from $546 \text{ J K}^{-1} \text{ kg}^{-1}$ at room temperature to $831 \text{ J K}^{-1} \text{ kg}^{-1}$ at liquidus temperature. Thermal conductivity varies from 7 to $33.4 \text{ W m}^{-1} \text{ K}^{-1}$ over the same temperature range. Thus, the temperature dependence of the properties dominates, which necessitates a coupling of the momentum equations with the energy equation and gives rise to strong nonlinearity in the conservation equations.

The variable properties have two effects on the numerical solution procedure [Ferziger & Peric, 2002]. First, although an incompressible flow assumption is made, the thermo-physical properties need to be kept inside the differential operators. Thus, solution methods for incompressible flow can be used. Second, the momentum and energy conservation equations have to be solved in a coupled way. In this study, the coupling between momentum and energy equations is achieved by the following iterative scheme:

1. Equations (1) - (3) and the related boundary conditions are solved iteratively using a two-step projection method [Chorin, 1968] to obtain velocities and pressures.

Thermo-physical properties used in this step are computed from the old temperature field. At each time step, the discretized momentum equations calculate new velocities in terms of an estimated pressure field. Then the pressure field is iteratively adjusted and velocity changes induced by each pressure correction are added to the previous velocities. This iterative process is repeated until the continuity equation is satisfied under an imposed tolerance by the newly computed velocities. This imposes a requirement for solving a linear system of equations. The preconditioned Bi-CGSTAB method [Barrett et al., 1994] is used to solve the linear system of equations.

Table 1. Material Properties for Ti-6Al-4V and Main Process Parameters

Physical Properties	Value
Liquidus temperature (K)	1923.0
Solidus temperature (K)	1877.0
Evaporation temperature (K)	3533.0
Solid specific heat ($J kg^{-1} K^{-1}$)	$\begin{cases} 483.04 + 0.215T & T \leq 1268K \\ 412.7 + 0.1801T & 1268 < T \leq 1923 \end{cases}$
Liquid specific heat ($J kg^{-1} K^{-1}$)	831.0
Thermal conductivity ($W m^{-1} K^{-1}$)	$\begin{cases} 1.2595 + 0.0157T & T \leq 1268K \\ 3.5127 + 0.0127T & 1268 < T \leq 1923 \\ -12.752 + 0.024T & T > 1923 \end{cases}$
Solid density ($kg m^{-3}$)	$4420 - 0.154 (T - 298 K)$
Liquid density ($kg m^{-3}$)	$3920 - 0.68 (T - 1923 K)$
Latent heat of fusion ($J kg^{-1}$)	2.86×10^5
Latent heat of evaporation ($J kg^{-1}$)	9.83×10^6
Dynamic viscosity ($N m^{-1} s^{-1}$)	3.25×10^{-3} (1923K)
	3.03×10^{-3} (1973K)
	2.66×10^{-3} (2073K)
	2.36×10^{-3} (2173K)
Radiation emissivity	$0.1536 + 1.8377 \times 10^{-4} (T - 300.0 K)$
Surface tension ($N m^{-1}$)	$1.525 - 0.28 \times 10^{-3} (T - 1941K)^a$
Thermal expansion coefficient (K^{-1})	1.1×10^{-5}
Laser absorption coefficient	0.4
Ambient temperature (K)	300
Convective coefficient ($W m^{-2} K^{-1}$)	10

^aValue for commercially pure titanium was used.

2. Equation (4) is solved by a method [Knoll et al., 1999] based on a finite volume discretization of the enthalpy formulation of Eq. (4). The finite volume approach ensures that the numerical scheme is locally and globally conservative, while the enthalpy formulation can treat phase change in a straightforward and unified manner. Once new temperature field is obtained, the thermo-physical properties are updated.
3. Equation (15) is solved using the PLIC-VOF [Gueyffier et al., 1999; Scardovelli & Zaleski, 2000, 2003] to obtain the updated free surface and geometry of the melt pool.
4. Advance to the next time step and back to step 1 until the desired process time is reached.

The time step is taken at the level of 10^{-6} s initially and adapted subsequently according to the convergence and stability requirements of the Courant–Friedrichs–Lewy (CFL) condition, the explicit differencing of the Newtonian viscous stress tensor, and the explicit treatment of the surface tension force.

3. SIMULATION RESULTS AND MODEL VALIDATION

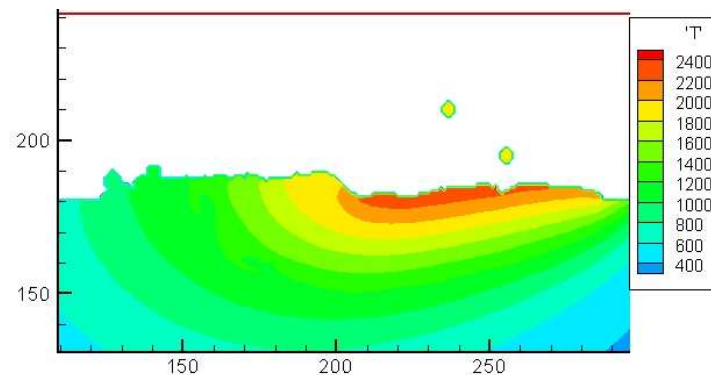
The parameters for the simulation were chosen based on the capability of our experimental facilities to compare the simulation results with the experimental measurements. A diode laser deposition system (the LAMP system of Missouri S&T) and a YAG laser deposition system at South Dakota School of Mines and Technology (SDSMT) were used for simulations and experiments. Ti-6Al-V4 plates with a thickness of 0.25 inch were selected as substrates. Ti-6Al-V4 powder particles with a diameter

from 40 to 140 μm were used as deposit material. Figure 3 shows the typical simulation results for temperature, velocity and VOF function.

The numerical model was validated from different aspects. First, it was validated in terms of melt pool peak temperature and melt pool length. The experiments were performed on the LAMP system as shown in Figure 4. The system consists of a diode laser, powder delivery unit, 5-axis CNC machine, and monitoring subsystem. The laser system used was a Nuvonyx ISL-1000M Diode Laser that is rated for 1 kW of output power. The laser emits at 808 nm and operates in the continuous wave (CW) mode. The laser spot size is 2.5 mm. To protect oxidization of Ti-6Al-V4, the system is covered in an environmental chamber to supply argon gas. The melt pool peak temperature is measured by a non-contact optical pyrometer that is designed for rough conditions, such as high ambient temperatures or electromagnetic interferences. A laser sight within the pyrometer allows for perfect alignment and focal length positioning; the spot size is 2.6 mm which encompasses the melt pool. The pyrometer senses the maximum temperature between 400 and 2500 (degrees C) and correlates the emissivity of the object to the resulting measurement. Temperature measurements are taken in real-time at 500 or 1000 Hz using a National Instruments real-time control system. A 4-20 mA signal is sent to the real-time system which is converted to degrees Celsius, displayed to the user and simultaneously recorded to be analyzed at a later date. Due to the collimator, the pyrometer is mounted to the Z-axis of the CNC at 42 (degrees) and is aligned with the center of the nozzle. Temperature measurements recorded the rise and steady state temperatures and the cooling rates of the melt pool. A complementary metal oxide semiconductor (CMOS) camera was installed right above the nozzle head for a better

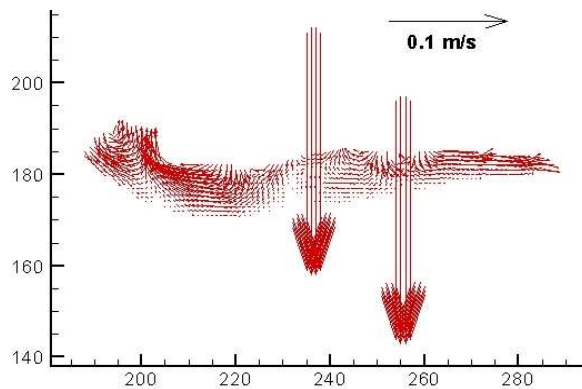
view in dynamically acquiring the melt pool image. The melt pool dimensions can be calculated from the image by the image process software.

Figure 5 and Figure 6 show the measured and predicted melt pool peak temperatures at different laser power levels and at different travel speeds, respectively. It can be seen from the plot that the general trend between simulation and experiment is consistent. At different power intensity level, there is a different error from 10 K (about 0.5%) to 121 K (about 5%). Figure 7 shows measured and predicted melt pool length at different laser power levels. The biggest disagreement between measured and simulated values is about 7%. It can be seen that the differences between measured and predicted values at higher power intensities (higher power levels or slower travel speeds) are generally bigger than those at lower power intensities. This can be explained by the two-dimensional nature of the numerical model. A 2D model does not consider the heat transfer in the third direction. At a higher power level, heat transfer in the third dimension is more significant.

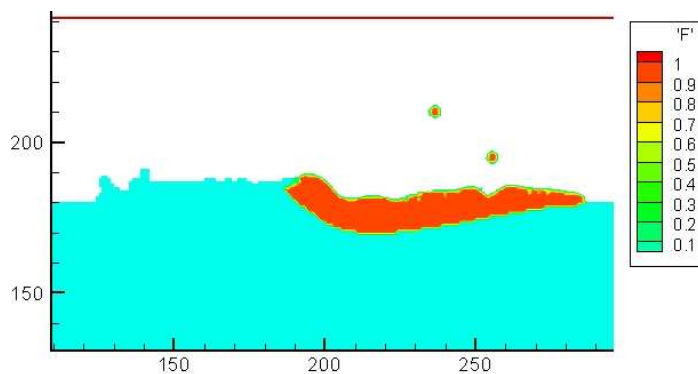


(a) Temperature field of the region around the melt pool

Figure 3. Simulation Results of Laser Deposition of Ti-6Al-4V



(b) Velocity field of the melt pool and falling powder particles



(c) VOF field of part of the region around the melt pool

Figure 3. Simulation Results of Laser Deposition of Ti-6Al-4V (Cont.)

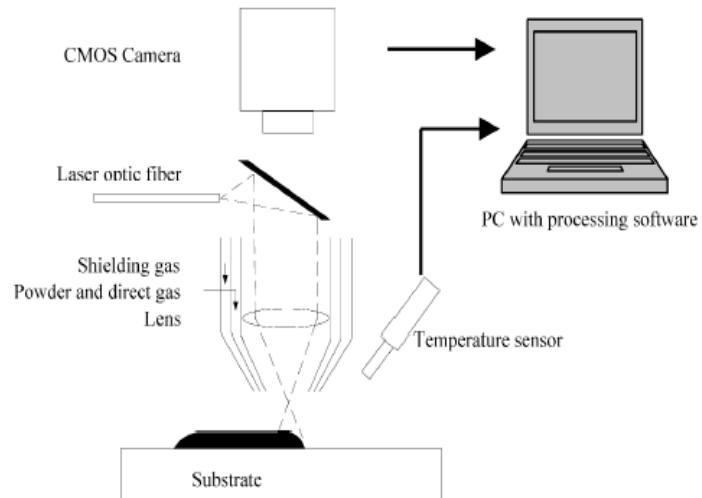


Figure 4. Schematic of Experimental Setup

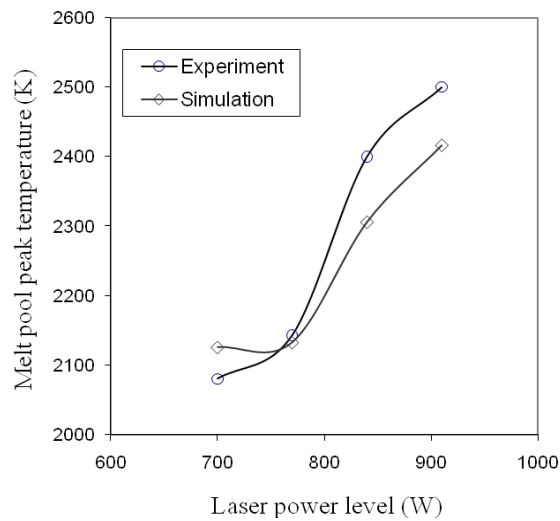


Figure 5. Melt Pool Peak Temperature Comparison between Simulation and Experiment at Different Laser Power Levels

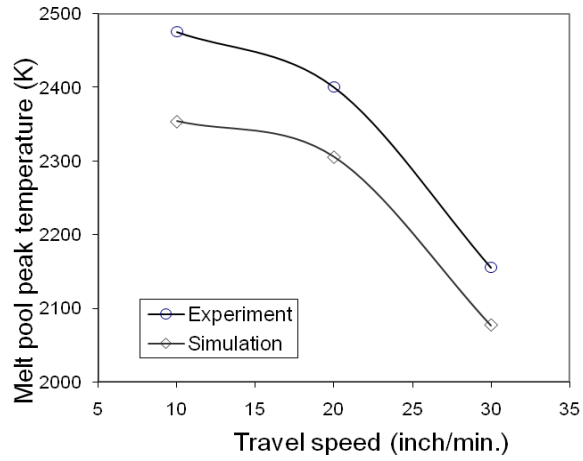


Figure 6. Melt Pool Peak Temperature Comparison between Simulation and Experiment at Different Travel Speeds

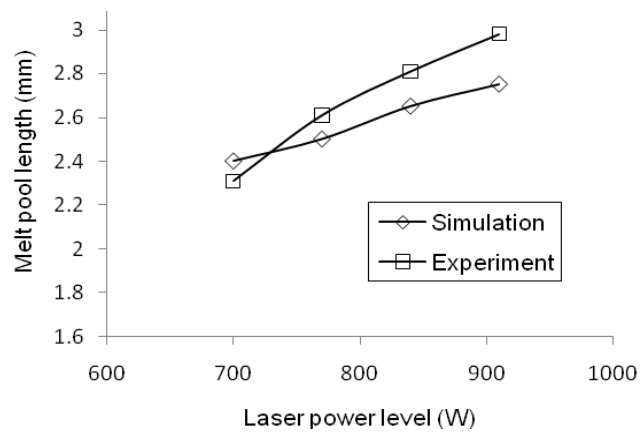


Figure 7. Melt Pool Length Comparisons between Simulation and Experiment at Different Power Levels

The samples were cross-sectioned using a Wire-EDM machine to measure dilution depth. An SEM (Scanning Electron Microscope) line trace was used to determine the dilution of the clad layer. The deposited Ti-6Al-4V is of Widmanstatten structure. The substrate has a rolled equi-axed alpha plus beta structure. Even though these two structures are easily distinguishable, the HAZ is large and has a martensitic structure that can be associated with it. Hence a small quantity of tool steel in the order of 5% was mixed with Ti-6Al-4V. The small quantity makes sure that it does not drastically change the deposit features of a 100% Ti-6Al-4V deposit. At the same time, the presence of Cr in tool steel makes it easily identifiable by means of EDS scans using SEM. Simulation and experimental results of dilution depth are shown in Figures 8 – 10.

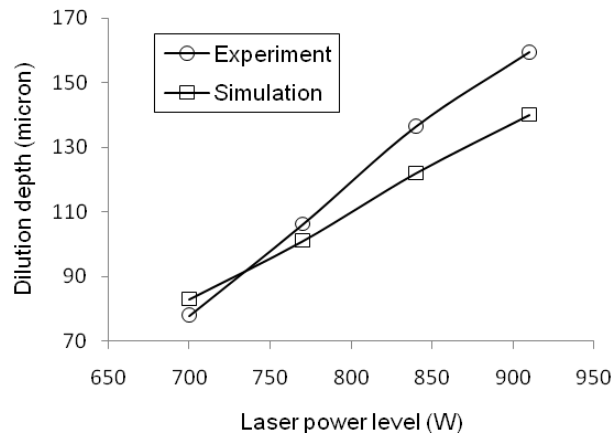


Figure 8. Comparison of Dilution Depth between Simulation and Experiment at Different Power Levels

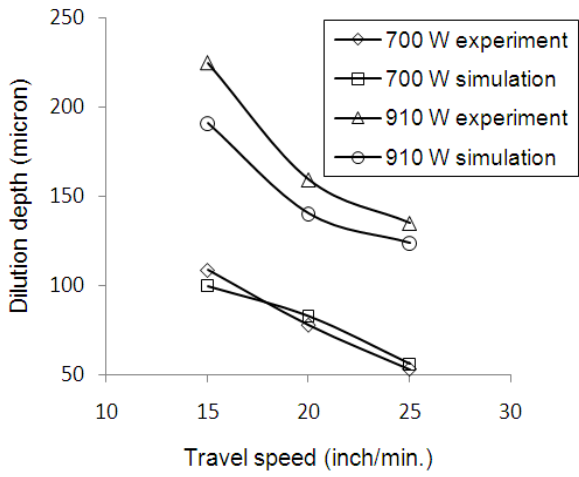


Figure 9. Comparison of Dilution Depth between Simulation and Experiment at Different Travel Speeds and Different Laser Power

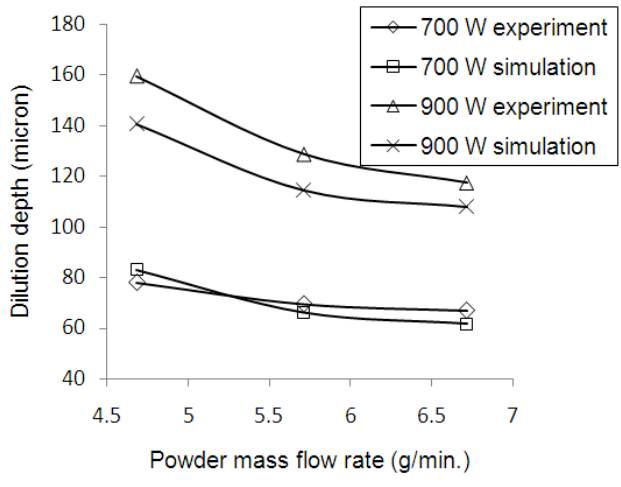


Figure 10. Comparison of Dilution Depth between Simulation and Experiment at Different Powder Mass Flow Rates and Different Laser Power Levels

Good agreements between measured and simulated dilution depths can be found in Figures 8-10. The differences are from about 4.8% to 15.1%. It can be seen that an increase in the laser power will increase the dilution depth. An increase in the laser travel speed will decrease the dilution depth. It is clear that the dilution depth has a linear dependence on the laser power and the laser travel speed. This is easy to understand. As the laser power increases, more power is available for melting the substrate. As travel speed decreases, the laser material interaction time is extended. From Figure 10, it can be seen that an increase in powder mass flow rate will decrease the dilution depth. But this effect is more significant at a higher level of laser power. It is likely that at a lower level of laser power, a significant portion of laser energy is consumed to melt the powder. Hence the energy available is barely enough to melt the substrate. Detailed discussion can be found in [Fan et al., 2006, 2007b; Fan, 2007].

Finally, the numerical model was validated in terms of its capability for predicting the lack-of-fusion defect. The test was performed using the YAG laser deposition system at South Dakota School of Mines and Technology (SDSMT). The simulation model determined that 1,200 watts would be the nominal energy level for the test. This means that based on the model, lack of fusion should occur when the laser power is below 1200W. In accordance with the test matrix, seven energy levels were tested: nominal, nominal $\pm 10\%$, nominal $\pm 20\%$, and nominal $\pm 30\%$. Based on the predicted nominal value of 1,200 watts, the seven energy levels in the test matrix are 840, 960, 1080, 1200, 1320, 1440, and 1540 watts. The deposited Ti-6Al-4V specimens were inspected at Quality Testing Services Co. using ultrasonic and radiographic inspections to determine the extent of lack-of-fusion in the specimens. The determination of whether or not there

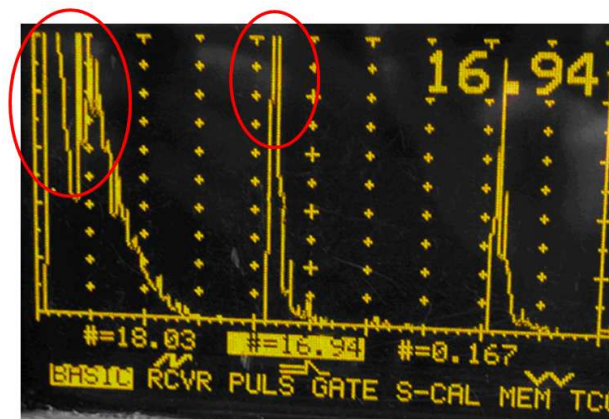
exists lack of fusion in a deposited specimen can be explained using Figure 11. First a substrate without deposit on it was inspected as shown in Figure 11 (a). Notice that the distance between two peaks are the thickness of the substrate. Then laser deposited specimens were inspected. If there is lack of fusion in a deposited specimen, some form of peaks can be found between the two high peaks in the ultrasonic graph, the distance of which is the height of the deposition and the thickness of the substrate. Fig. 11 (b) shows an ultrasonic graph of a deposited specimen with a very good deposition. The ultrasonic result indicates there is not lack of fusion occurring between layers and the interface. The distance between two peaks is the height of the deposition and the thickness of the substrate. For the deposition as shown in Figure 11 (c), the lack of fusion occurs as the small peak (in circle) appears between two high peaks. The results revealed that no lack-of-fusion was detected in specimens deposited using 1,200 watts and higher energy levels. However, lack-of-fusion was detected in specimens deposited from lower energy levels (minus 10% up to minus 30% of 1,200 watts.). The test results validated the simulation model.

4. CONCLUSIONS

This chapter has outlined the approach for mathematical and numerical modeling of fusion-based additive manufacturing of titanium. The emphasis is put on modeling of transport phenomena associated with the process, including heat transfer and fluid flow dynamics. Of particular interest are the modeling approaches for solidification and free surface flow with surface tension. The advantages and disadvantages of the main

modeling approaches are briefly discussed. Based on the comparisons, the continuum model is adopted for modeling of melting/solidification phase change, and the VOF method for modeling of free-surface flow in the melt pool.

The laser deposition process is selected as an example of fusion-based additive manufacturing processes. The governing equations, auxiliary relationships, and boundary conditions for the solidification system and free-surface flow are presented. The main challenge for modeling of the surface tension-dominant free surface flow is discussed and the measures to overcome the challenge are given. The numerical implementation procedures are outlined, with a focus on the effects of variable material property on the discretization schemes and solution algorithms. Finally the simulation results are presented and compared with experimental measurements. A good agreement has been obtained and thus the numerical model is validated. The modeling approach can be applied to other fusion-based manufacturing processes, such as casting and welding.



(a) Ultrasonic Graph of a Ti-6Al-4V Substrate

Figure 11. Ultrasonic Graphs of a Laser Deposited Ti-6Al-4V Specimen



(b) Ultrasonic Graph of a Laser Deposited Ti-6Al-4V Specimen
without Lack of Fusion



(c) Ultrasonic Graph of a Laser Deposited Ti-6Al-4V Specimen
with Lack of Fusion

Figure 11. Ultrasonic Graphs of a Laser Deposited Ti-6Al-4V Specimen (Cont.)

5. ACKNOWLEDGEMENTS

This research was partially supported by the National Aeronautics and Space Administration Grant Number NNX11AI73A, the grant from the U.S. Air Force Research Laboratory, and Missouri S&T's Intelligent Systems Center and Manufacturing Engineering program. Their support is greatly appreciated. The help from Dr. Kevin Slattery and Mr. Hsin Nan Chou at Boeing-St Louis and Dr. James Sears at South Dakota School of Mines and Technology are also acknowledged.

6. REFERENCES

- Aulisa, E.; Manservigi, S.; Scardovelli, R. & Zaleski, S. (2007). Interface reconstruction with least-squares fit and split advection in three-dimensional Cartesian geometry, *Journal of Computational Physics*, Vol. 225, No.2, (August 2007), pp. 2301-2319, ISSN 0021-9991
- Barrett, R.; Berry, M.; Chan, T. F.; Demmel, J.; Donato, J.; Dongarra, J.; Eijkhout, V.; Pozo, R.; Romine, C. & Van der Vorst, H. (1994). *Templates for the Solution of Linear Systems: Building Blocks for Iterative Methods* (2nd Edition), SIAM, ISBN 978-0-898713-28-2 Philadelphia, PA
- Beckermann C. & Viskanta, R. (1988). Double-diffusive convection during dendritic solidification of a binary mixture. *PCH: Physicochemical Hydrodynamics*, Vol. 10, No.2, pp. 195-213, ISSN 0191-9059
- Beckermann, C.; Diepers, H.-J.; Steinbach, I.; Karma, A. & Tong X. (1999). Modeling Melt Convection in Phase-Field Simulations of Solidification, *Journal of Computational Physics*, Vol. 154, No.2, (September 1999), pp. 468–496, ISSN 0021-9991
- Benes, J. (2007). Cool Tips for Cutting Titanium, In: *American Machinist*, 26.09.2011, Available from <http://www.americanmachinist.com/304/Issue/Article/False/77297/>
- Bennon, W. D. & Incropera, F. P. (1987). A continuum model for momentum, heat and species transport in binary solid-liquid phase change systems-I. Model formulation. *International Journal of Heat and Mass Transfer*, Vol. 30, No. 10, (October 1987), pp. 2161-2170, ISSN 0017-9310

- Benson, D.J. (2002). Volume of fluid interface reconstruction methods for multi-material problems. *Applied Mechanics Reviews*, Vol. 55, No. 2, (March 2002), pp. 151–165, ISSN 0003-6900
- Bhat, M. S.; Poirier, D.R. & Heinrich, J.C. (1995). Permeability for cross flow through columnar-dendritic alloys. *Metallurgical and Materials Transactions B*, Vol. 26, No.5, (October 1995), pp. 1049-1092, ISSN 1073-5615
- Boettinger, W.J.; Coriell, S. R.; Greer, A. L.; Karma, A.; Kurz, W.; Rappaz, M. & Trivedi, R. (2000). Solidification microstructures: recent developments, future directions, *Acta Materialia*, Vol. 48, No.1, (January 2000), pp. 43-70, ISSN 1359-6454
- Boettinger, W. J.; Warren, J. A.; Beckermann, C. & Karma, A. (2002). Phase-Field Simulation of Solidification, *Annual Review of Materials Research*, Vol. 32, pp. 163-194, ISSN 1531-7331
- Boyer, R; Welsch, G. & Collings, E.W. (1994). *Materials properties handbook: titanium alloys*, ASM International, ISBN 978-0871704818, Materials Park, OH
- Brackbill, J.U.; Kothe, D.B. & Zemach, C. (1992). A continuum method for modeling surface tension, *Journal of Computational Physics*, Vol. 100, No.2, (June 1992), pp. 335–354, ISSN 0021-9991
- Caboussat, A. (2005). Numerical Simulation of Two-Phase Free Surface Flows. *Archives of Computational Methods in Engineering*, Vol. 12, No.2, (June 2005), pp. 165-224, ISSN 1134-3060
- Carman, P.C. (1937). Fluid flow through granular beds. *Transactions of the Institution of Chemical Engineers*, Vol. 15, (February 1937), pp. 150-166, ISSN 0046-9858
- Caginalp, G. (1989). Stefan and Hele-Shaw type models as asymptotic limits of the phase-field equations. *Physical Review A*, Vol.39, No.11, (June 1989), pp. 5887-5896, ISSN 1050-2947
- Choi, M.; Greif, R. & Salcudean, M. (1987). A study of the heat transfer during arc welding with applications to pure metals or alloys and low or high boiling temperature materials, *Numerical Heat Transfer*, Vol. 11, No.4, (April 1987) pp. 477-491, ISSN 0149-5720
- Chorin, A.J. (1968). Numerical solution of the Navier-Stokes equations. *Mathematics of Computation*, Vol. 22, No. 104, (October 1968), pp. 745-762, ISSN 0025-5718
- Chorin, A.J. (1980). Flame advection and propagation algorithms, *Journal of Computational Physics*, Vol. 35, No. 1, (March 1980), pp. 1–11, ISSN 0021-9991

- Clyne, T. W. & Kurz, W. (1981). Solute redistribution during solidification with rapid solid state diffusion. *Metallurgical Transactions A*, Vol.12, No.6, (June 1981), pp. 965–971, ISSN 1073-5623
- Cummins, S. J.; Francois, M. M. & Kothe, D.B. (2005). Estimating curvature from volume fractions. *Computers & Structures*, Vol.83, No. 6-7, (February 2005), pp. 425–434, ISSN 0045-7949
- Debar, R. (1974). *Fundamentals of the KRAKEN Code*, Technical Report UCIR-760, Lawrence Livermore National Laboratory, 1974
- Drummond, J. E. & Tahir, M.I. (1984). Laminar viscous flow through regular arrays of parallel solid cylinders. *International Journal of Multiphase Flow*, Vol. 10, No. 5, (October 1984), pp. 515–540, ISSN 0301-9322
- Eylon, D. & Froes, F.H. (1984). Titanium Net-Shape Technologies. *Journal of Metals*, Vol. 36, No. 6, (June 1984), pp. 36-41, ISSN 1047-4838
- Fan,Z.; Sparks, T.E.; Liou, F.; Jambunathan, A.; Bao, Y.; Ruan, J. & Newkirk, J.W. (2007). Numerical Simulation of the Evolution of Solidification Microstructure in Laser Deposition. *Proceedings of the 18th Annual Solid Freeform Fabrication Symposium*, Austin, TX, USA, August 2007
- Fan,Z.; Stroble,J.K.; Ruan, J.; Sparks, T.E. & Liou, F. (2007). Numerical and Analytical Modeling of Laser Deposition with Preheating. *Proceedings of ASME 2007 International Manufacturing Science and Engineering Conference*, ISBN 0-7918-4290-8, Atlanta, Georgia, USA, October, 2007, pp. 37-51
- Fan,Z. (2007). *Numerical and Experimental Study of Parameter Sensitivity and Dilution in Laser Deposition*, Master Thesis, University of Missouri-Rolla, 2007
- Fan,Z.; Jambunathan, A.; Sparks, T.E.; Ruan, J.; Yang, Y.; Bao, Y. & Liou, F. (2006). Numerical simulation and prediction of dilution during laser deposition. *Proceedings of the 17th Annual Solid Freeform Fabrication Symposium*, Austin, TX, USA, August 2006, pp. 532-545
- Ferziger, J.H. & Peric, M. (2002). *Computational Methods for Fluid Dynamics* (3rd edition), Springer-Verlag, ISBN 3-540-42074-6, Berlin Heidelberg New York
- Francois, M.M.; Cummins, S.J.; Dendy, E.D.; Kothe, D.B.; Sicilian, J.M. & Williams, M.W. (2006). A balanced-force algorithm for continuous and sharp interfacial surface tension models within a volume tracking framework. *Journal of Computational Physics*, Vol. 213, No. 1, (March 2006), pp. 141–173, ISSN 0021-9991

- Frenk, A.; Vandyoussefi, M.; Wagniere, J.; Zryd, A. & Kurz, W. (1997). Analysis of the laser-cladding process for stellite on steel. *Metallurgical and Materials Transactions B*, Vol. 28, No.3, (June 1997), pp. 501-508, ISSN 1073-5615
- Fuster, D.; Agbaglah, G.; Josserand, C.; Popinet, S. & Zaleski, S. (2009). Numerical simulation of droplets, bubbles and waves: state of the art. *Fluid Dynamics Research*, Vol.41, No.6, (December 2009), p. 065001 (24 pp.), ISSN 0169-5983
- Gandin, Ch.-A. & Rappaz, M. (1994). A coupled finite element-cellular automaton model for the prediction of dendritic grain structures in solidification processes, *Acta Metallurgica et Materialia*, Vol. 42, No. 7, (July 1994), pp. 2233-2246, ISSN 0956-7151
- Ganesan, S. & Poirier, D. R. (1990). Conservation of mass and momentum for the flow of interdendritic liquid during solidification, *Metallurgical Transactions B*, Vol. 21, No.1, (February 1990), pp. 173-181, ISSN 1073-5615
- Ganesan, S.; Chan, C.L. & Poirier, D.R. (1992). Permeability for flow parallel to primary dendrite arms. *Materials Science and Engineering: A*, Vol. 151, No. 2, (May 1992), pp. 97-105, ISSN 0921-5093
- Gerlach, D.; Tomar, G.; Biswas, G. & Durst, F. (2006). Comparison of volume-of-fluid methods for surface tension-dominant two-phase flows. *International Journal of Heat and Mass Transfer*, Vol. 49, No. 3-4, (February 2006), pp. 740-754, ISSN 0017-9310
- Gibou, F.; Fedkiw, R.; Caflisch, R. & Osher, S. (2003). A Level Set Approach for the Numerical Simulation of Dendritic Growth. *Journal of Scientific Computing*, Vol. 19, No.1-3, (December 2003), pp. 183-199, ISSN 0885-7474
- Grujicic, M.; Cao, G. & Figliola, R.S. (2001). Computer simulations of the evolution of solidification microstructure in the LENSTM rapid fabrication process, *Applied Surface Science*, Vol. 183, No. 1-2, (November 2001), pp. 43-57, ISSN 0169-4332
- Gueyffier, D.; Li, J.; Nadim, A.; Scardovelli, R. & Zaleski, S. (1999). Volume of Fluid interface tracking with smoothed surface stress methods for three-dimensional flows. *Journal of Computational Physics*, Vol. 152, No.2, (July 1999), pp. 423-456, ISSN 0021-9991
- Hansbo, P. (2000). A Free-Lagrange Finite Element Method using Space-Time Elements. *Computer Methods in Applied Mechanics and Engineering*, Vol. 188, No. 1-3, (July 2000), pp. 347-361, ISSN 0045-7825
- Hills, R.N.; Loper, D.E. & Roberts, P.H. (1983). A thermodynamically consistent model of a mushy zone. *The Quarterly Journal of Mechanics & Applied Mathematics*, Vol. 36, No. 4, (November 1983), pp. 505-536, ISSN 0033-5614

- Hirt, C.W. & Nichols, B.D. (1981). Volume-of-fluid (VOF) for the dynamics of free boundaries. *Journal of Computational Physics*, Vol. 39, No.1, (January 1981), pp. 201-225, ISSN 0021-9991
- Hirt, C. W. & Nichols, B. D. (1988). *Flow-3D user manual*, Technical Report, Flow Sciences, Inc.
- Idelsohn, S. R.; Storti, M. A. & Onate, E. (2001). Lagrangian Formulations to Solve Free Surface Incompressible Inviscid Fluid Flows. *Computer Methods in Applied Mechanics and Engineering*, Vol. 191, No. 6-7, (December 2001), pp. 583–593, ISSN 0045-7825
- Jacqmin, D. (1999). Calculation of two-phase Navier–Stokes flows using phase-field modeling. *Journal of Computational Physics*, Vol. 155, No.1, (October 1999), pp. 96–127, ISSN 0021-9991
- Jaluria, Y. (2006). Numerical Modeling of Manufacturing Processes. In: *Handbook of Numerical Heat Transfer* (2 edition), Minkowycz, W.J.; Sparrow, E.M. & Murthy, J.Y., (Ed.), pp. 729-783, Wiley, ISBN 0471348783, Hoboken, New Jersey
- Jones, W.P. & Launder, B.E. (1973). The calculation of low-Reynolds-number phenomena with a two-equation model of turbulence. *International Journal of Heat and Mass Transfer*, Vol. 16, No. 6, (June 1973), pp.1119-1130, ISSN 0017-9310
- Juric D. & Tryggvason G. (1996). A Front-Tracking Method for Dendritic Solidification, *Journal of Computational Physics*, Vol. 123, No.1, (January 1996) pp. 127–148, ISSN 0021-9991
- Karma, A. & Rappel, W.J. (1996). Phase-field method for computationally efficient modeling of solidification with arbitrary interface kinetics, *Physical Review E*, Vol. 53, No.4, (April 1996), pp. R3017-R3020, ISSN 1063-651X
- Karma, A. & Rappel, W.J. (1998). Quantitative phase-field modeling of dendritic growth in two and three dimensions. *Physical Review E*, Vol. 57, No.4, (April 1998), pp. 4323-4329, ISSN 1063-651X
- Kim, Y.T.; Goldenfeld, N. & Dantzig, J. (2000). Computation of dendritic microstructures using a level set method. *Physical Review E*, Vol. 62, No.2, (August 2000). pp. 2471-2474, ISSN 1063-651X
- Knoll, D. A.; Kothe, D. B. & Lally, B. (1999). A new nonlinear solution method for phase change problems. *Numerical Heat Transfer, Part B Fundamentals*, Vol. 35, No. 4, (December 1999), pp. 436–459, ISSN 1040-7790
- Kobayashi, R. (1993). Modeling and numerical simulations of dendritic crystal growth. *Physica D: Nonlinear Phenomena*, Vol. 63, No. 3-4, (March 1993), pp. 410-423, ISSN 0167-2789

- Kobryn, P.A.; Ontko, N.R.; Perkins, L.P. & Tiley, J.S. (2006) Additive Manufacturing of Aerospace Alloys for Aircraft Structures. In: *Cost Effective Manufacture via Net-Shape Processing*, Meeting Proceedings RTO-MP-AVT-139, Neuilly-sur-Seine, France: RTO, pp. 3-1 – 3-14
- Kothe, D. B.; Mjolsness, R. C. & Torrey, M. D. (1991). *RIPPLE: A Computer Program for Incompressible Flows with Free surfaces*, Technical Report, LA-12007-MS, Los Alamos National Lab
- Lafaurie, B.; Nardone, C.; Scardovelli, R.; Zaleski, S. & Zanetti, G. (1994). Modelling Merging and Fragmentation in Multiphase Flows with SURFER. *Journal of Computational Physics*, Vol. 113, No.1, (July 1994), pp. 134-147, ISSN 0021-9991
- Liou, F. & Kinsella, M. (2009). A Rapid Manufacturing Process for High Performance Precision Metal Parts. *Proceedings of RAPID 2009 Conference & Exposition*, Society of Manufacturing Engineers, Schaumburg, IL, USA, May 2009
- Liovic, P.; Francois, M.; Rudman, M. & Manasseh, R. (2010). Efficient simulation of surface tension-dominated flows through enhanced interface geometry interrogation. *Journal of Computational Physics*, Vol. 229, No. 19, (September 2010), pp. 7520-7544, ISSN 0021-9991
- Lips, T. & Fritsche, B. (2005). A comparison of commonly used re-entry analysis tools, *Acta Astronautica*, Vol. 57, No.2-8, (July-October 2005), pp. 312-323, ISSN 0094-5765
- López, J. & Hernández, J. (2010). On reducing interface curvature computation errors in the height function technique. *Journal of Computational Physics*, Vol.229, No.13, (July 2010), pp. 4855-4868, ISSN 0021-9991
- Meier, M; Yadigaroglu, G. & Smith, B.L. (2002). A novel technique for including surface tension in PLIC-VOF methods. *European Journal of Mechanics - B/Fluids*, Vol. 21, No. 1, ISSN 0997-7546, pp. 61-73, ISSN 0997-7546
- Mills, K. C. (2002). *Recommended Values of Thermophysical Properties for Selected Commercial Alloys*, Woodhead Publishing Ltd, ISBN 978-1855735699, Cambridge
- Muller, I.A. (1968). A Thermodynamic theory of mixtures of fluids, *Archive for Rational Mechanics and Analysis*, Vol. 28, No. 1, (January 1968), pp. 1-39, ISSN 0003-9527
- Ni, J. & Beckermann, C. (1991). A volume-averaged two-phase model for transport phenomena during solidification, *Metallurgical Transactions B*, Vol. 22, No.3, (June 1991), pp. 349-361, ISSN 1073-5615

- Ni, J. & Incropera, F. P. (1995). Extension of the Continuum Model for Transport Phenomena Occurring during Metal Alloy Solidification, Part I: The Conservation Equations. *International Journal of Heat and Mass Transfer*, Vol. 38, No. 7, (May 1995), pp. 1271-1284, ISSN 0017-9310
- Nichols, B. D.; Hirt, C. W. & Hotchkiss, R. S. (1980). *SOLA-VOF: A solution algorithm for transient fluid flow with multiple free boundaries*, Technical Report, LA-8355, Los Alamos National Lab
- Noh, W.F. & Woodward, P.R. (1976). SLIC (simple line interface calculation), *Lecture Notes in Physics*, Vol. 59, pp. 330–340, ISSN 0075-8450
- Pavlyk, V. & Dilthey, U. (2004). Numerical Simulation of Solidification Structures During Fusion Welding. In: *Continuum Scale Simulation of Engineering Materials: Fundamentals - Microstructures - Process Applications*, Raabe, D.; Franz Roters, F.; Barlat, F. & Chen, L.Q., (Ed.), pp. 745-762, Wiley, ISBN 978-3-527-30760-9, Weinheim, Germany
- Pilliod Jr., J.E. & Puckett, E.G. (2004). Second-order accurate volume-of-fluid algorithms for tracking material interfaces. *Journal of Computational Physics*, Vol. 199, No. 2, (September 2004), pp. 465–502, ISSN 0021-9991
- Poirier, D.R. (1987). Permeability for flow of interdendritic liquid in columnar-dendritic alloys. *Metallurgical Transactions B*, Vol. 18, No. 1, (March 1987), pp. 245-255, ISSN 1073-5615
- Prantil, V. C. & Dawson, P. R. (1983). Application of a mixture theory to continuous casting. In: *Transport Phenomena in Materials Processing*, Chen, M. M.; Mazumder, J. & Tucker III, C. L., (Ed.), pp. 469-484, ASME, ISBN 978-9994588787, New York, N.Y.
- Prescott, P.J.; Incropera, F.P. & Bennon, W.D. (1991). Modeling of Dendritic Solidification Systems: Reassessment of the Continuum Momentum Equation. *International Journal of Heat and Mass Transfer*, Vol. 34, No. 9, (September 1991), pp. 2351-2360, ISSN 0017-9310
- Provatas, N.; Goldenfeld, N. & Dantzig, J. (1998). Efficient Computation of Dendritic Microstructures using Adaptive Mesh Refinement. *Physical Review Letters*, Vol. 80, No. 15, (April 1998), pp. 3308-3311, ISSN 0031-9007
- Ramaswamy, B. & Kahawara, M. (1987). Lagrangian finite element analysis applied to viscous free surface fluid flow. *International Journal for Numerical Methods in Fluids*, Vol. 7, No. 9, (September 1987), pp. 953-984, ISSN 0271-2091

- Rappaz, M. & Gandin, Ch.-A. (1993). Probabilistic modelling of microstructure formation in solidification processes. *Acta Metallurgica Et Materialia*, vol. 41, No. 2, (February 1993), pp. 345-360, ISSN 0956-7151
- Renardy Y. & Renardy, M. (2002). PROST: A parabolic reconstruction of surface tension for the volume-of-fluid method. *Journal of Computational Physics*, Vol. 183, No. 2, (December 2002), pp. 400–421, ISSN 0021-9991
- Rider, W.J. & Kothe, D.B. (1998). Reconstructing volume tracking. *Journal of Computational Physics*, Vol. 141, No. 2, (April 1998), pp. 112–152, ISSN 0021-9991
- Rudman, M. (1997). Volume-tracking methods for interfacial flow calculations. *International Journal for Numerical Methods in Fluids*, Vol. 24, No.7, (April 1997), pp.671-691, ISSN 0271-2091
- Scardovelli, R. & Zaleski, S. (1999). Direct numerical simulation of free-surface and interfacial flow, *Annual Review of Fluid Mechanics*, Vol. 31, (January 1999), pp. 567-603, ISSN 0066-4189
- Scardovelli R. & Zaleski S. (2000). Analytical relations connecting linear interfaces and volume fractions in rectangular grids, *Journal of Computational Physics*, Vol. 164, No. 1, (October 2000), pp. 228-237, ISSN 0021-9991
- Scardovelli, R. & Zaleski, S. (2003). Interface Reconstruction with Least-Square Fit and Split Eulerian-Lagrangian Advection. *International Journal for Numerical Methods in Fluids*, Vol. 41, No.3, (January 2003), pp. 251-274, ISSN 0271-2091
- Scheil, E. (1942). *Z. Metallkd*, Vol.34, pp. 70-72, ISSN 0044-3093
- Sethian, J. A. (1996). *Level Set Methods: Evolving Interfaces in Computational Geometry, Fluid Mechanics, Computer Vision, and Materials Science*, Cambridge University Press, ISBN 978-0521572026, Cambridge, UK.
- Sethian, J. A. (1999). *Level Set Methods and Fast Marching Methods: Evolving Interfaces in Computational Geometry, Fluid Mechanics, Computer Vision, and Materials Science* (2 edition), Cambridge University Press, ISBN 978-0521645577, Cambridge, UK.
- Shirani, E.; Ashgriz, N. & Mostaghimi, J. (2005). Interface pressure calculation based on conservation of momentum for front capturing methods. *Journal of Computational Physics*, Vol. 203, No. 1, (February 2005), pp. 154–175, ISSN 0021-9991
- Stefanescu, D.M. (2002). *Science and Engineering of Casting Solidification*, Springer, ISBN 030646750X, New York, NY

- Steinbach, I.; Pezzolla, F.; Nestler, B.; Seeszelberg, M.; Prieler, R.; Schmitz G.J. & Rezende J.L.L. (1996). A phase field concept for multiphase systems. *Physica D*, Vol. 94, No.3, (August 1996), pp. 135-147, ISSN 0167-2789
- Sullivan Jr., J. M.; Lynch, D.R. & O'Neill, K. (1987) Finite element simulation of planar instabilities during solidification of an undercooled melt. *Journal of Computational Physics*, Vol. 69, No. 1, (March 1987), pp. 81-111, ISSN 0021-9991
- Swaminathan, C. R. & Voller, V. R. (1992). A general enthalpy method for modeling solidification processes. *Metallurgical Transactions B*, Vol. 23, No. 5, (October 1992), pp. 651-664, ISSN 1073-5615
- Takizawa, A.; Koshizuka, S. & Kondo S. (1992). Generalization of physical component boundary fitted co-ordinate method for the analysis of free surface flow. *International Journal for Numerical Methods in Fluids*, Vol. 15, No. 10, (November 1992), pp. 1213-1237, ISSN 0271-2091
- Tang, H.; Wrobel, L.C. & Fan, Z. (2004). Tracking of immiscible interfaces in multiple-material mixing processes, *Computational Materials Science*, Vol. 29, No.1, (January 2004), pp.103–118, ISSN 0927-0256
- Torrey, M. D.; Cloutman, L. D.; Mjolsness, R. C. & Hirt, C. W. (1985). *NASA-VOF2D: a computer program for incompressible flow with free surfaces*, Technical Report, LA-101612-MS, Los Alamos National Lab
- Torrey, M. D.; Mjolsness, R. C. & Stein L. R. (1987). *NASA-VOF3D: a three-dimensional computer program for incompressible flow with free surfaces*, Technical Report, LA-11009-MS, Los Alamos National Lab
- Tryggvason, G.; Bunner, B.; Esmaeeli, A.; Juric, D.; Al-Rawahi, N.; Tauber, W.; Han, J.; Nas, S. & Jan, Y.-J. (2001). A Front-Tracking Method for the Computations of Multiphase Flow. *Journal of Computational Physics*, Vol. 169, No. 2, (May 2001), pp. 708–759, ISSN 0021-9991
- Udaykumar, H. S.; Mittal, R. & Shyy, W. (1999). Computation of Solid–Liquid Phase Fronts in the Sharp Interface Limit on Fixed Grids. *Journal of Computational Physics*, Vol. 153, No.2, (August 1999), pp. 535–574, ISSN 0021-9991
- Udaykumar, H.S.; Marella, S. & Krishnan, S. (2003). Sharp-interface simulation of dendritic growth with convection: benchmarks. *International Journal of Heat and Mass Transfer*, Vol. 46, No.14, (July 2003), pp. 2615-2627, ISSN 0017-9310
- Voller, V.R. & Prakash, C. (1987). A Fixed Grid Numerical Modeling Methodology for Convection-Diffusion Mushy Region Phase Change Problems. *International Journal of Heat and Mass Transfer*, Vol. 30, No. 8, (August 1987), pp. 1709-1719, ISSN 0017-9310

- Voller, V.R.; Brent, A. & Prakash, C. (1989). The Modeling of Heat, Mass and Solute Transport in Solidification Systems, *International Journal of Heat and Mass Transfer*, Vol. 32, No. 9, (September 1989), pp. 1719-1731, ISSN 0017-9310
- Voller, V.R.; Mouchmov, A. & Cross, M. (2004). An explicit scheme for coupling temperature and concentration fields in solidification models. *Applied Mathematical Modelling*, Vol. 28, No. 1, (January 2004), pp. 79–94, ISSN 0307-904X
- Voller, V.R. (2006). Numerical Methods for Phase-Change Problems. In: *Handbook of Numerical Heat Transfer* (2 edition), Minkowycz, W.J.; Sparrow, E.M. & Murthy, J.Y., (Ed.), pp. 593-622, Wiley, ISBN 978-0-471-34878-8, Hoboken, New Jersey
- Warren, J.A. & Boettinger, W.J. (1995) Prediction of dendritic growth and microsegregation patterns in a binary alloy using the phase-field method. *Acta Metallurgica et Materialia*, Vol. 43, No. 2, (February 1995), pp. 689-703, ISSN 0956-7151
- West, R. (1985). On the permeability of the two-phase zone during solidification of alloys. *Metallurgical and Materials Transactions A*, Vol. 16, No. 4, (April 1985), pp. 693, ISSN 1073-5623
- Wheeler, A.A.; Boettinger, W.J. & McFadden, G.B. (1992). Phase-field model for isothermal phase transitions in binary alloys. *Physical Review A*, Vol. 45, No. 10, (May 1992), pp. 7424 -7439, ISSN 1050-2947
- Youngs, D.L. (1982). Time-dependent multi-material flow with large fluid distortion. In: *Numerical Methods for Fluid Dynamics*, Morton, K.W. & Baines, M. J. (Ed.), pp. 273–285, Academic Press, ISBN 9780125083607, UK
- Youngs, D.L. (1984). *An Interface Tracking Method for a 3D Eulerian Hydrodynamics Code*, Technical Report 44/92/35, AWRE, 1984
- Yu, K.O. & Imam, M.A. (2007). Development of Titanium Processing Technology in the USA. *Proceedings of the 11th World Conference on Titanium (Ti-2007)*, Kyoto, Japan, June 2007
- Zhu, M. F.; Lee, S. Y. & Hong, C. P. (2004). Modified cellular automaton model for the prediction of dendritic growth with melt convection. *Physical Review E*, Vol. 69, No.6, (June 2004), pp. 061610-1 - 061610-12, ISSN 1063-651X

II. NUMERICAL AND ANALYTICAL MODELING OF LASER DEPOSITION WITH PREHEATING

ABSTRACT

Laser deposition allows quick fabrication of fully-dense metallic components directly from CAD solid models. This work uses both numerical and analytical approaches to model the laser deposition process including actual deposition and preheating. The numerical approach is used to simulate the coupled, interactive transport phenomena during actual deposition. The numerical simulation involves laser material interaction, free surface evolution, and melt-pool dynamics. The analytical approach is used to model heat transfer during preheating. The combination of these two approaches can increase computational efficiency with most of the phenomena associated with laser deposition modeled. The simulation is applied to Ti-6Al-4V and simulation results are compared with experimental results.

1. INTRODUCTION

Laser deposition is an extension of the laser cladding process. This additive manufacturing technique allows quick fabrication of fully-dense metallic components directly from Computer Aided Design (CAD) solid models. The applications of laser deposition include rapid prototyping, rapid tooling and part refurbishment. As shown in Figure 1, laser deposition uses a focused laser beam as a heat source to create a melt pool

on an underlying substrate. Powder material is then injected into the melt pool through nozzles. The incoming powder is metallurgically bonded with the substrate upon solidification. The part is fabricated in a layer by layer manner in a shape that is dictated by the CAD solid model.

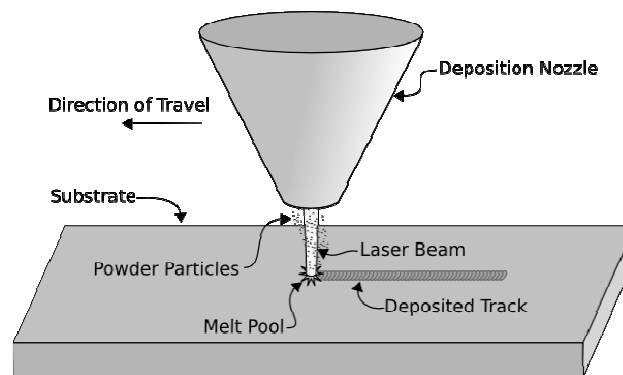


Figure 1. Schematic of a Typical Laser Deposition System

During the laser deposition process, several defects, such as porosity and cracks, should be paid attention to. Cracks initiate corrosion fracture and reduce fatigue strength of the deposited parts. Cracks are caused by the residual stresses created by the high thermal gradient built up during the cooling stage. Residual stresses can be reduced by a reduction of the cooling rate. This can be achieved by preheating the substrate. Moreover, the preheating causes a better absorption of the laser beam and further it is possible to

melt more powder in the larger melting pool and enhance the bonding. Usually the preheating is performed in such a manner that a very small melting of the substrate material occurs without powder injection.

Thermal analysis of the laser deposition process is very important for optimization of the process. If the substrate surface temperatures remain too low, wetted deposit material is limited. In that case, irregularly shaped tracks with a lot of cracks, porosity and a poor bonding, are produced. However, if too high substrate surface temperatures are reached, severe melting of the substrate occurs. The high degree of dilution can deteriorate the clad properties. A comprehensive numerical model has been developed that allows the prediction of temperature distribution and melt pool dynamics. This model simulate the coaxial laser deposition process with powder injection, and considers most of the associated phenomena, such as melting, solidification, evaporation, evolution of the free surface, and powder injection. Input parameters for this model are laser machining parameters and properties of the laser beam, as well as material properties and the laser beam absorption. To get more accurate predictions, finer grid needs to be used. This, together with the iterative nature of the numerical algorithms, causes the model computationally to not be very efficient. In this paper an analytical model is applied to the preheating process (without powder injection) to increase the computational efficiency, while the actual deposition process with powder injection still uses the numerical model. The outputs of the analytical model, i.e. the temperature distribution of the substrate, are used as the initial conditions of the numerical model.

In this study, a coaxial diode laser deposition system is considered for simulations and experiments. The blown powder method is used to deliver powder. Diode laser is

believed to have a number of process advantages as opposed to the CO₂ or Nd:YAG laser, including the better material coupling efficiency (laser absorption) and better beam profile (non Gauss-shape intensity distribution) for laser deposition. Material of both powder and substrates is Ti-6Al-4V, which is widely used in the aerospace industry.

The rest of the paper is organized as follows: In Section 2 and 3, the numerical model and the analytical model are presented, respectively. In Section 4, simulation results are compared to the experimental results, and discussions are made. In Section 5 conclusions are completed.

2. NUMERICAL MODEL

2.1 Governing Equations. Figure 2 shows a schematic diagram of the calculation domain, including the substrate, melt pool, remelted zone, deposited layer and part of the gas region. In laser deposition, melting and solidification cause the phase transformation at the solid/liquid interface. A mushy zone containing solid and liquid is formed. In this study the continuum model [1, 2] is adopted to derive the governing equations.

The assumptions for the system of governing equations include: (1) the fluid flow in the melt pool is a Newtonian, incompressible, laminar flow; (2) the solid and liquid phases in the mushy zone are in local thermal equilibrium; (3) the solid phase is rigid; and (4) isotropic permeability exists. For the system of interest, the conservation equations for mass, momentum and energy are summarized as follows:

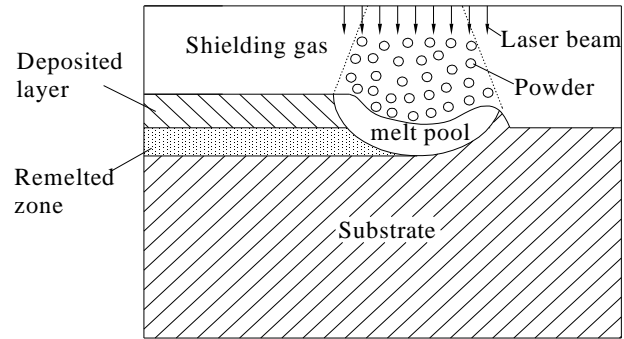


Figure 2. Schematic of the Calculation Domain

Continuity

$$\frac{\partial \rho}{\partial t} + \nabla \cdot (\rho \vec{V}) = 0 \quad (1)$$

Momentum

$$\frac{\partial}{\partial t} (\rho \vec{V}) + \nabla \cdot (\rho \vec{V} \vec{V}) = \nabla \cdot \left(\mu_l \frac{\rho}{\rho_l} \nabla \vec{V} \right) - \nabla p - \frac{\mu_l}{K} \frac{\rho}{\rho_l} (\vec{V} - \vec{V}_s) + \rho \vec{g} + S \quad (2)$$

Energy

$$\frac{\partial(\rho h)}{\partial t} + \nabla \cdot (\rho \vec{V} h) = \nabla \cdot (k \nabla T) - \nabla \cdot (\rho (h_l - h) (\vec{V} - \vec{V}_s)) \quad (3)$$

In Equations (1) - (3), the continuum density, thermal conductivity, vector velocity, enthalpy, as well as specific heat to be used later are defined as follows:

$$\begin{aligned} \rho &= g_s \rho_s + g_l \rho_l & k &= g_s k_s + g_l k_l & \vec{V} &= f_s \vec{V}_s + f_l \vec{V}_l \\ h &= f_s h_s + f_l h_l & c &= f_s c_s + f_l c_l \end{aligned} \quad (4)$$

The liquid fraction temperature relationship is given by:

$$g_l = \begin{cases} 0 & \text{if } T < T_s \\ \frac{T - T_s}{T_l - T_s} & \text{if } T_s \leq T \leq T_l \\ 1 & \text{if } T > T_l \end{cases} \quad (5)$$

The other volume and mass fractions can be obtained by:

$$\begin{aligned} f_l &= \frac{g_l \rho_l}{\rho} & f_s &= \frac{g_s \rho_s}{\rho} \\ g_s + g_l &= 1 & f_s &= 1 - f_l \end{aligned} \quad (6)$$

The phase enthalpy for the solid and the liquid can be expressed as:

$$h_s = \int_0^T c_s(T)dT \quad h_l = \int_0^{T_s} c_s(T)dT + \int_{T_s}^T c_l(T)dT + L_m \quad (7)$$

where L_m is the latent heat of melting.

Permeability, K , is assumed to vary with liquid volume fraction according to the Carman-Kozeny equation[3] derived from Darcy's law:

$$K = \frac{g_l^3}{C(1-g_l)^2} \quad (8)$$

where the parameter C is a constant depending on the morphology and size of the dendrites in the mushy zone. The S is a source term that will be defined in Section 2.4.

2.2 Tracking of the Solid/Liquid Interface. The solid/liquid interface is implicitly tracked by the continuum model [1, 2]. In the solid phase region and liquid phase region, the third term on the right-hand side of Equation (2) vanishes. This is because in the solid phase region $\vec{V} = \vec{V}_s = 0$ and in liquid phase region $K \rightarrow \infty$ since $g_l = 1$. So this term is only valid in the mushy zone.

2.3 Tracking of the Free Surface. The liquid/vapor interface, or the free surface of the melt pool, is very complex due to surface tension, thermocapillary force, and impaction of the powder injection. In this study, the Volume-Of-Fluid (VOF) method [4] is employed to track the evolution of the moving free surface of the melt pool. The melt pool configuration is defined in terms of a volume of fluid function, $F(x,y,t)$, which represents the volume of fluid per unit volume and satisfies the conservation equation:

$$\frac{\partial F}{\partial t} + (V \cdot \nabla)F = 0 \quad (9)$$

2.4 Formulation of Source Term. The source term, S , in the momentum equation is contributed by the interface forces acting on the free surface, such as surface tension, etc. In this study, the continuum surface force (CSF) model [5] is used to reformulate the surface force. In its standard form, surface tension is formulated as [5]:

$$\vec{F}_s(\bar{x}_s) = \hat{n}\gamma\kappa + \nabla_s\gamma \quad (10)$$

where $\vec{F}_s(\bar{x}_s)$ is the net surface force at a point \bar{x}_s on a interface S . \hat{n} is a unit normal to S at the point \bar{x}_s , which is given by:

$$\hat{n} = \frac{\vec{n}}{|\vec{n}|} \quad (11)$$

where \vec{n} is the surface normal vector and can be computed from the gradient of the VOF function:

$$\vec{n} = \nabla F \quad (12)$$

∇_s is the gradient along a direction tangential to the interface, which is defined as:

$$\nabla_s = \nabla - \nabla_N = \nabla - \hat{n}(\hat{n} \cdot \nabla) \quad (13)$$

γ and κ represent surface tension coefficient and curvature, respectively. κ is given in [6]:

$$\kappa = -(\nabla \cdot \hat{n}) = \frac{1}{|\bar{n}|} \left[\left(\frac{n}{|\bar{n}|} \cdot \nabla \right) |\bar{n}| - (\nabla \cdot \bar{n}) \right] \quad (14)$$

By using the CSF model, the surface force \vec{F}_s is reformulated into a volume force \vec{F}_b as follows:

$$\vec{F}_b = \vec{F}_s |\bar{n}| \frac{F}{\langle F \rangle} = \vec{F}_s |\nabla F| \frac{F}{\langle F \rangle} \quad (15)$$

where $\langle F \rangle$ is the averaged F value across the free surface. Thus, the source term S in equation (2) is formulated as:

$$S = (\bar{n} \gamma \kappa + \nabla_s \gamma) |\nabla F| \frac{F}{\langle F \rangle} \quad (16)$$

2.5 Boundary Conditions. The boundary conditions at the free surface satisfy the following equation:

$$k \frac{\partial T}{\partial n} = \frac{\eta(P_{laser} - P_{atten})}{\pi R^2} - h_c(T - T_\infty) - \varepsilon \sigma(T^4 - T_\infty^4) - \dot{m}_e L_v \quad (17)$$

where terms on the right-hand side are laser irradiation, convective heat loss, radiation heat loss and evaporation heat loss, respectively. P_{laser} is the power of laser beam, P_{atten} the power attenuated by the powder cloud, R is the laser beam radius, η the laser absorption coefficient. P_{atten} is calculated according to Frenk's et al. model [7] with a minor modification:

$$P_{atten} = P_{laser} \left[1 - \exp \left(- \frac{3Q_{ext} \dot{m} l}{\pi \rho r_p D_{jet} v_p} \right) \right] \quad (18)$$

where \dot{m} denotes the powder mass flow rate, l is the stand-off distance from the nozzle exit to the substrate, ρ is powder density, r_p is the radius of the powder particle, D_{jet} is the diameter of the powder jet, v_p is the powder injection velocity, and Q_{ext} is the extinction coefficient. It is assumed that the extinction cross section is close to the actual geometrical cross section, and Q_{ext} takes a value of unity. In the evaporation term, \dot{m}_e is the evaporation mass flux and L_v is the latent heat of evaporation. According to Choi et al.'s "overall evaporation model" [8], \dot{m}_e is of the form:

$$\log \dot{m}_e = A + 6.1210 - \frac{18836}{T} - 0.5 \log T \quad (19)$$

where A is a constant dependent on the material.

The boundary conditions at the bottom, left and right wall satisfy the following equations:

$$k \frac{\partial T}{\partial n} = -h_c (T - T_\infty) \quad (21)$$

$$u = 0 \quad v = 0 \quad (22)$$

2.6 Numerical Algorithm. The governing equations (Equations (1)-(3), and (10)) and all related supplemental equations and boundary conditions are solved through the following iterative scheme:

1. Equations (1)-(2) and the related boundary conditions are solved iteratively using the SOLA-VOF algorithm [9] to obtain velocities and pressures. At each time step, the discretized momentum equations calculate new velocities in terms of an estimated pressure field. Then the pressure field is iteratively adjusted and velocity changes induced by each pressure correction are added to the previous velocities. The residue of conservation equations is selected as error criteria. The iterative process is repeated until a tolerance of 10^{-5} is met.

2. The energy equation (4) is solved by an implicit method.

3. Equation (10) is solved to obtain the updated free surface and geometry of the melt pool.

4. Advance to the next time step and back to step 1 until the desired process time is reached.

In this scheme, staggered grids are employed where the temperatures, pressures and VOF function are located at the cell center and the velocities at the walls. The source

term in the momentum is obtained at grid points that are located in the transition region. A fixed grid is used and grid independence of the simulations occurs at mesh size =10 μ m in the sense that the maximum deviation between the results for mesh size =10 μ m and mesh size =5 μ m is observed to be less than 0.5%. Thus, the solution does not improve much beyond mesh size of 10 μ m. The time step is taken at the level of 10⁻⁶s initially and adapted subsequently according to the convergence and stability requirements of the SOLA-VOF algorithm [9], the CSF model [5], and the numerical solution for the energy equation.

3. ANALYTICAL MODEL

In this work, Komanduri and Hou's model [10], which is based on moving heat source theory of Jaeger [11] and Carslaw and Jaeger [12], is utilized to get the analytical solution for the temperature distribution in preheating of the substrate. The analytical model is almost identical to the one developed by Komanduri and Hou [10] and hence some details will be omitted. In [10], the width of the substrate (perpendicular to the laser scanning direction) is assumed to be large enough so that the effects of widthwise boundaries is negligible.

3.1 Solution of a Disc Heat Source with a Uniform Intensity Distribution, Moving on the Surface of a Semi-infinite Medium. Follow Komanduri and Hou's work [10], the temperature rise of a point M(x, y, z) at any time t after the initiation of the heat source in a semi-infinite medium due to a disc heat source is given by:

$$\Delta T = \frac{P}{2c\rho(4\pi\alpha)^{3/2}} \int_0^t \frac{d\tau}{\tau^{3/2}} \exp\left(-\frac{r_0^2 + X^2 + y^2 + z^2}{4\alpha\tau}\right) \cdot \exp\left(-\frac{Xv}{2\alpha}\right) \cdot \exp\left(-\frac{v^2\tau}{4\alpha}\right) \cdot I_0\left(\frac{r_0}{2\alpha\tau} \sqrt{(X + v\tau)^2 + y^2}\right) \quad (23)$$

where y, z are coordinates in the absolute coordinate system, while X is the corresponding moving coordinate. P is the laser power absorbed by the substrate. r_0 is the radius of the disc heat source, v its moving velocity, I_0 the modified Bessel function of the first kind, order zero. c, ρ , α are specific heat, density and thermal diffusivity, respectively. Let $R^2 = r_0^2 + X^2 + y^2 + z^2$, Eq. (23) becomes:

$$\Delta T = \frac{P}{2c\rho(4\pi\alpha)^{3/2}} \int_0^t \frac{d\tau}{\tau^{3/2}} \exp\left(-\frac{R^2}{4\alpha\tau}\right) \cdot \exp\left(-\frac{Xv}{2\alpha}\right) \cdot \exp\left(-\frac{v^2\tau}{4\alpha}\right) \cdot I_0\left(\frac{r_0}{2\alpha\tau} \sqrt{(X + v\tau)^2 + y^2}\right) \quad (24)$$

3.2 Solution of a Disc Heat Source with a Uniform Intensity Distribution,

Considering the Boundary Conditions of the Bottom and Side Surfaces. Here the bottom and the lengthwise side surfaces are considered as adiabatic. Using the image method, five image heat sources are considered. The temperature rise at any point M is the sum of the effects from all the primary and the image heat sources which are located away from the point M at distances of $R_0, R_1, R_2, R_3, R_4, R_5$, respectively. Suppose the substrate has the dimensions $H \times L \times W$, H is the height of the substrate, L is the length

of substrate in the heat source moving direction. The values of these distances and their projections on the X-axis are given in Table 1.

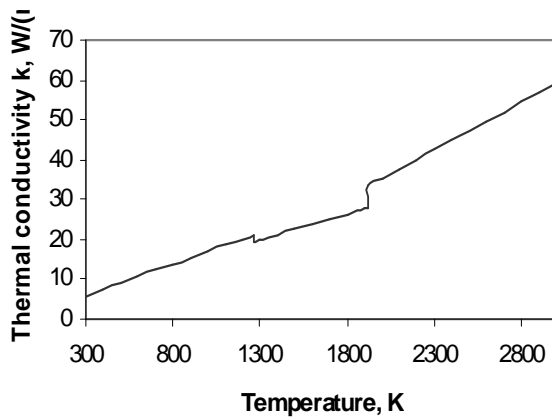
Table 1 Distances and Their Projections

S	Value of Distance	Sym	Value of
R	$\sqrt{X^2 + y^2 + z^2}$	X ₀	X
R	$\sqrt{X^2 + y^2 + (2H - z)^2}$	X ₁	X
R	$\sqrt{(X + 2vt)^2 + y^2 + z^2}$	X ₂	-(X + 2vt)
R	$\sqrt{(X + 2vt)^2 + y^2 + (2H - z)^2}$	X ₃	-(X + 2vt)
R	$\sqrt{(2(L - vt) - X)^2 + y^2 + z^2}$	X ₄	2(L - vt) - X
R	$\sqrt{(2(L - vt) - X)^2 + y^2 + (2H - z)^2}$	X ₅	2(L - vt) - X

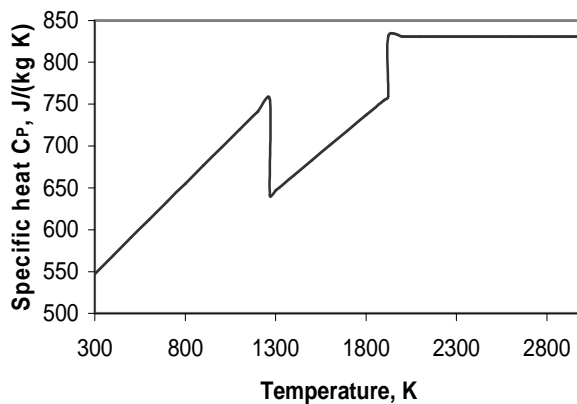
The temperature rise at any point M caused by the primary heat source is given by Equation (24), and the temperature rise at any point M caused by each of the image heat source is obtained by substituting the aforementioned values of the distances and their relevant projections on the X-axis instead of R and X in Equation (24).

3.3 Temperature Consideration for Thermo-Physical Properties. This analytical solution can not consider variable thermal properties with temperature, as it would complicate the mathematical analysis [10]. Consider temperature dependent thermal properties of Ti-6Al-4V, as shown in Figure 3. Because we are interested in thermal properties in the temperature range from 300 K to 2500 K, in this study the

thermal properties are taken at 1923 K. The rationale for this choice is that the thermal conductivity at 1923 K is nearly the average from 300K to 2500 K and the specific heat above this temperature is constant.



(a) Thermal Conductivity as a Function of Temperature for Ti-6Al-4V



(b) Specific Heat as a Function of Temperature for Ti-6Al-4V

Figure 3. Thermal Conductivity and Specific Heat as a Function of Temperature for Ti-6Al-4V [13]

4. NUMERICAL SIMULATION AND EXPERIMENTS

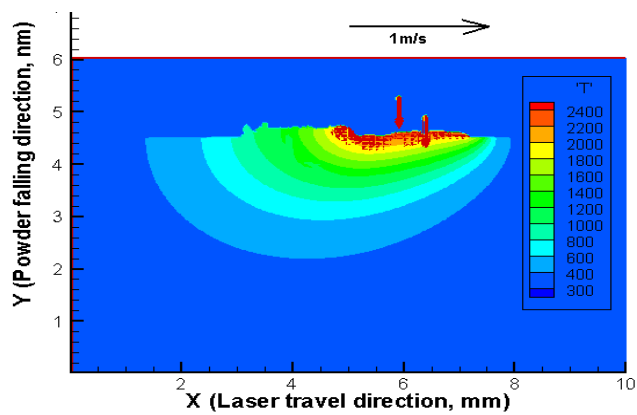
4.1 Numerical Simulation. Simulation is performed based on the capability of our experimental facilities to compare the simulation results with the experimental measurements. A continuous wave diode laser with an 808 nm wavelength is considered as the energy source. The laser intensity distribution is uniform. For substrates, Ti-6Al-V4 plates with a thickness of 0.25 inch are selected. Ti-6Al-V4 powder particles with a diameter from 40 to 140 μm are used as deposit material. The laser absorption coefficient is measured by Sparks et al. [14]. The material properties and the main process parameters are shown in Table 2. Figure 4 shows the typical simulation results for temperature, velocity and VOF function.

4.2 Experiments. The experiments were performed on the LAMP system shown in Figure 5. The system consists of a diode laser, powder delivery unit, 5-axis CNC machine, and monitoring subsystem. The laser system used in the study was Nuvonyx (Nuvonyx Inc.) ISL-1000M Laser Diode System which combines state-of-the-art micro-optics with laser diodes to produce the only single wavelength fiber coupled direct diode laser at power levels up to 1000 watts CW. The laser emits at 808 nm and operates in the continuous wave (CW) mode. To protect oxidization of Ti-6Al-V4, the system is covered in an environmental chamber to supply argon gas for titanium deposition. For the other aspects of the system architecture, refer to Liou et al. [17] and Boddu et al. [18]. The substrates have dimensions of 2.5 (Length) \times 5 (Width) \times 0.4 (Thickness) in.

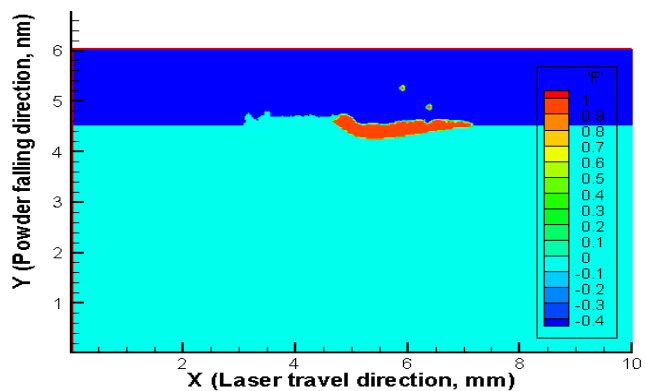
The melt pool temperature is measured by a non-contact optical pyrometer that is designed for rough conditions, such as high ambient temperatures or electromagnetic interferences. A laser sight within the pyrometer allows for perfect alignment and focal

Table 2. Material Properties for Ti-6Al-4V and Main Process Parameters

Nonmenclature	Symbol	Value (unit)
Melting temperature	T_m	1900.0K
Liquidus temperature	T_l	1923.0K
Solidus temperature	T_s	1877.0K
Evaporation temperature	T_v	3533.0K
Solid specific heat at constant pressure [13]	c_{ps}	$\begin{cases} 483.04 + 0.215T & T \leq 1268K \\ 412.7 + 0.1801T & 1268 < T \leq 1923 \end{cases} \quad J/kg \cdot K$
Liquid specific heat at constant pressure [15]	c_{pl}	831.0 J/kg K
Thermal conductivity [13]	k	$\begin{cases} 1.2595 + 0.0157T & T \leq 1268K \\ 3.5127 + 0.0127T & 1268 < T \leq 1923 \\ -12.752 + 0.024T & T > 1923 \end{cases} \quad W/m \cdot K$
Solid density [15]	ρ_s	$4420 - 0.154(T - 298 \text{ K})$
Liquid density [15]	ρ_l	$3920 - 0.68(T - 1923 \text{ K})$
Latent heat of fusion [15]	L_m	$2.86 \times 10^5 \text{ J/kg}$
Latent heat of evaporation	L_v	$9.83 \times 10^6 \text{ J/kg}$
Dynamic viscosity	μ	$3.25 \times 10^{-3} \text{ N/m s (1923K)}$ $3.03 \times 10^{-3} \text{ (1973K)}$ $2.66 \times 10^{-3} \text{ (2073K)}$ $2.36 \times 10^{-3} \text{ (2173K)}$
Radiation emissivity [16]	ε	$0.1536 + 1.8377 \times 10^{-4}(T - 300.0 \text{ K})$
Laser absorption coefficient [13]	η	0.4
Powder particle diameter	D_p	40-140 μm
Shielding gas pressure	P_g	5 psi
Ambient temperature	T_∞	300K
Convective coefficient	h_c	10 W/m ² K



(a) Temperature and Velocity Fields



(b) Volume of Fluid Field

Figure 4. Simulation Results at $t = 225$ ms

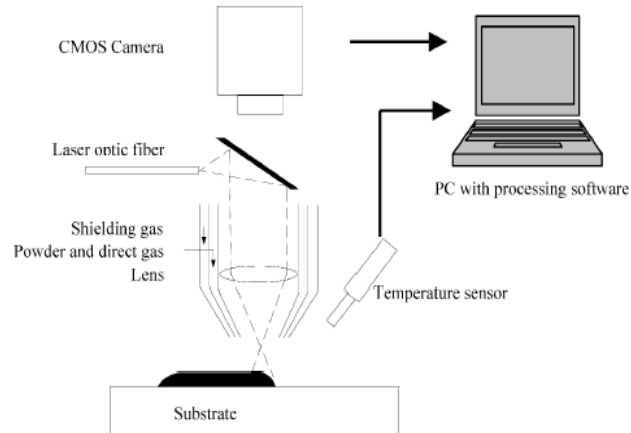


Figure 5. Schematic of Experimental Setup

length positioning; the spot size is 2.6 mm which encompasses the melt pool. The pyrometer senses the maximum temperature between 400 and 2500 °C and correlates the emissivity of the object to the resulting measurement. Temperature measurements are taken in real-time at 500 or 1000 Hz using a National Instruments real-time control system. A 4-20 mA signal is sent to the real-time system which is converted to degrees Celsius, displayed to the user and simultaneously recorded to be analyzed at a later date. Due to the collimator, the pyrometer is mounted to the Z-axis of the CNC at 42 (degrees) and is aligned with the center of the nozzle. Temperature measurements for the aforementioned experiments recorded the rise and steady state temperatures and the cooling rates of the melt pool.

To measure dilution depth, the laser deposited samples are cut using a Wire-EDM machine. After samples are obtained from experiments conducted in the setup shown in Figure 5, an SEM (Scanning Electron Microscope) line trace is used on each of the

samples to determine the dilution of the clad layer. The deposited Ti-6Al-4V typically consists of a Widmanstätten structure. The substrate has a rolled equi-axed alpha+ beta structure. Even though these two structures are considerably different and are easily distinguishable, the HAZ is large and has a martensitic structure that can be associated with it. Hence, a small quantity of tool steel in the order of 5% was mixed with Ti-6Al-4V. The small quantity makes sure that it does not drastically change the deposit features of a 100 % Ti-6Al-4V deposit. At the same time, the presence of Cr in tool steel makes it easily identifiable by means of EDS scans using SEM. Knowing the exact location of Cr in the substrate would provide the depth of the melt pool in the substrate to measure dilution.

In order to validate the model predictions, single path deposition experiments are conducted. The comparisons between model predictions and experimental results are conducted in terms of melt pool peak temperature and dilution depth.

4.3 Comparisons and Discussions. Figure 6 and Figure 7 show the comparisons between experimental measurements and model predictions. Figure 6 shows the effects of laser power on melt pool peak temperature. It can be seen that an increase in the laser power will increase the melt pool temperature. This is easy to understand. As the laser power increases, more power is available for melting the substrate. Figure 7 shows the effects of laser scanning speed on the melt pool peak temperature. An increase in the laser scanning speed will decrease the melt pool peak temperature. This is because, as scanning speed decreases, the laser material interaction time is extended.

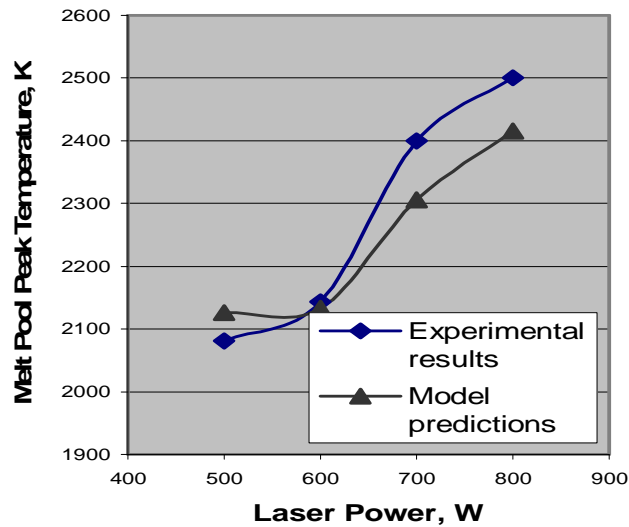


Figure 6. Comparisons between Experimental Measurements and Model Predictions at a Constant Powder Mass Flow Rate and a Constant Laser Scanning Speed

Simulation and experimental results of dilution depth are shown in Figures 8-10. Dilution depth depends on the energy absorbed by the substrate, given the specific material, the geometry of the substrate, laser beam spot size, and the beam profile. Laser power and laser travel speed determine the total energy density potentially absorbed by the substrate. Powder mass flow rate affects the energy actually absorbed by the substrate by the mechanism of power attenuation due to the powder cloud. Laser power, travel speed and powder mass flow rate are the three main process parameters to determine the dilution depth.

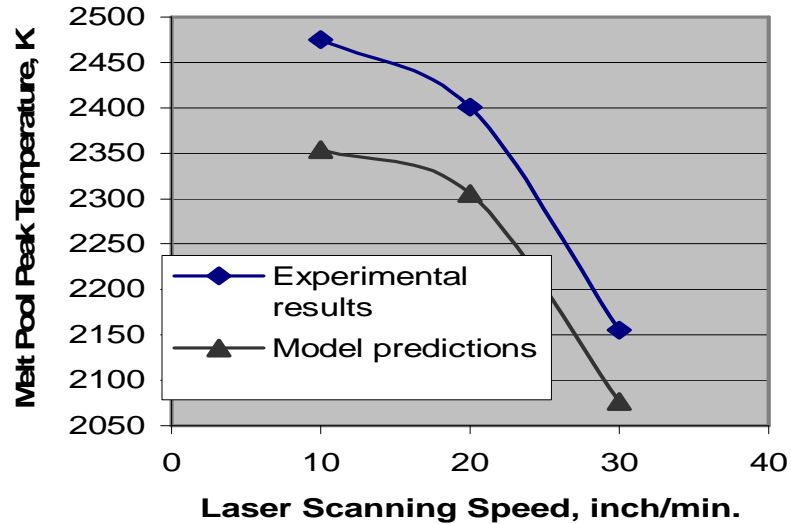


Figure 7. Comparisons between Experimental Measurements and Model Predictions at a Constant Powder Mass Flow Rate and a Constant Laser Power

From Figures 8-10, it can be seen that an increase in the laser power will increase the dilution depth. An increase in the laser travel speed will decrease the dilution depth. It is clear that the dilution depth has a linear dependence on the laser power and the laser travel speed. This is easy to understand. As the laser power increases, more power is available for melting the substrate. As travel speed decreases, the laser material interaction time is extended.

From Figure 10, it can be seen that an increase in powder mass flow rate will decrease the dilution depth. But this effect is more significant at a lower level of powder mass flow. It is likely that at a lower level of powder mass flow, the effect of powder mass flow rate on powder catchment efficiency is more significant. Also at a higher level

of laser power, the effect of powder mass flow rate on dilution depth is more significant. It is likely that at a higher level of laser power, on one hand more power is attenuated given a constant attenuation ratio and more power is absorbed by the powder; on the other hand, the deposited material can decrease the temperature gradients more significantly.

From Figures 6-10, we can see that the general trend between experimental measurements and model predictions is consistent. At different power intensity level, there is a different error from 10 K (about 0.5%) to 121K (about 5%). It can be seen that at higher power intensity level, there is a bigger error for melt pool peak temperature between measurements and predictions. This is because the numerical model is two-dimensional. It doesn't consider the heat and mass transfer in the third direction. At a higher power intensity level, heat and mass transfer in the third dimension is more significant. The errors between experimental measurements and model predictions are analyzed to mainly come from the following aspects: (1) The two-dimensional nature of the numerical model; (2) The thermo-physical properties taken for the analytical model; (3) The uncertainties of the material properties and the appropriateness of the sub-models for the numerical model; (4) Boundary conditions. Adiabatic boundary conditions are assumed in the analytical model and the numerical model for the bottom surface and side surfaces. Measurements also have been taken to achieve such boundary conditions in experiments. But it is hard to get absolute adiabatic boundary conditions. (5) The SEM measurement of the dilution depth may bring about some errors. This method described before may not be very accurate since it tracks the trend of Chromium distribution.

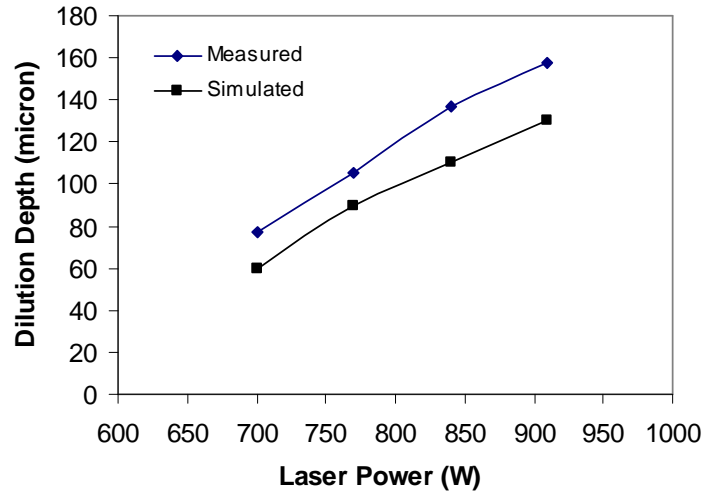


Figure 8. Dilution Depth as a Function of Laser Power

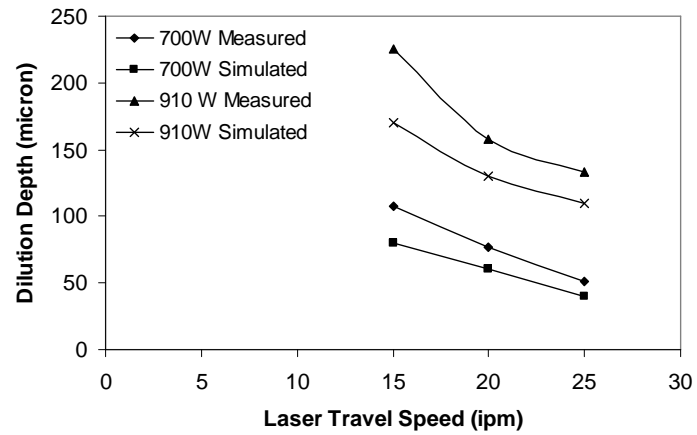


Figure 9. Dilution Depth as a Function of Laser Travel Speed

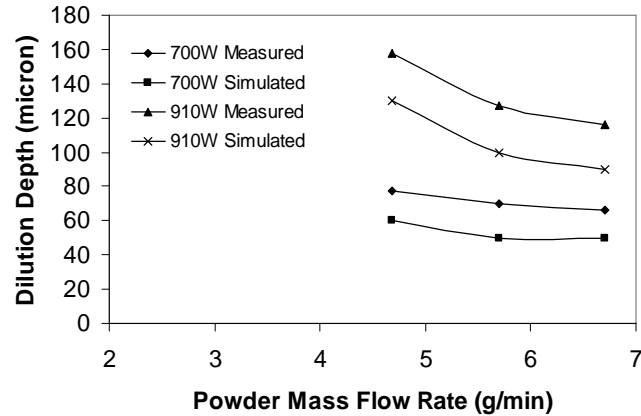


Figure 10. Dilution Depth as a Function of Powder Mass Flow Rate

5. CONCLUSIONS

An analytical model for thermal analysis of temperature rise due to a moving heat source is combined into a comprehensive heat transfer and fluid flow numerical model for the laser deposition process. The analytical model is used for the preheating process before the actual laser deposition with powder injection. And the numerical model is used for the actual laser deposition process. Thus the outputs of the analytical model are used as the inputs of the numerical model. Experiments have been done to validate the model predictions. A consistent general trend is found between experimental measurements and the model predictions. The sources of the errors have been analyzed.

6. ACKNOWLEDGEMENTS

This research was supported by the National Science Foundation grants DMI-9871185 and IIP-0637796, the grant from the U.S. Air Force Research Laboratory contract # FA8650-04-C-5704. The support from Boeing Phantom Works, Product Innovation and Engineering, LLC, Spartan Light Metal Products Inc, Missouri S&T Intelligent Systems Center, and Missouri S&T Manufacturing Engineering Program, is also greatly appreciated.

7. REFERENCES

- [1] W.D. Bennon, F.P. Incropera, A continuum model for momentum, heat and species transport in binary solid-liquid phase change systems-I. model formulation, *International Journal of Heat and Mass Transfer* 30 (1987) 2161-2170.
- [2] W.D. Bennon, F.P. Incropera, A continuum model for momentum, heat and species transport in binary solid-liquid phase-change systems--II. Application to solidification in a rectangular cavity, *International Journal of Heat and Mass Transfer* 30 (1987) 2171-2187.
- [3] P.C. Carman, Fluid flow through granular beds, *Trans. Institution Chem. Engrs.* 15 (1937) 150-166.
- [4] C.W. Hirt, B.D. Nichols, Volume of fluid (VOF) method for the dynamics of free boundaries, *Journal of Computational Physics* 39 (1981) 201-225.
- [5] J. U. Brackbill, D. B. Kothe, C. Zemach, A continuum method for modeling surface tension, *Journal of Computational Physics* 100 (1992) 335-354.
- [6] C. Prakash, V. Voller, On the numerical solution of continuum mixture model equations describing binary solid-liquid phase change, *Numerical Heat Transfer* 15B (1989) 171-89.
- [7] A. Frenk, M. Vandyoussefi, J. Wagniere, A. Zryd, W. Kurz, Analysis of the laser-cladding process for stellite on steel, *Metallurgical and Materials Transactions B (USA)* 28B (1997) 501-508.

- [8] M. Choi, R. Greif, M. Salcudean, A study of the heat transfer during arc welding with applications to pure metals or alloys and low or high boiling temperature materials, *Numerical Heat Transfer* 11 (1987) 477-491.
- [9] B. D. Nichols, C.W. Hirt, R. S. Hotchkiss, SOLA-VOF: A solution algorithm for transient fluid flow with multiple free boundaries, LA-8355, Los Alamos National Laboratory.
- [10] R.Komanduri, Z.B. Hou, Thermal analysis of the arc welding process. I. General solutions, *Metallurgical and Materials Transactions B (USA)*. Vol. 31B, no. 6, pp. 1353-1370B, 2000
- [11] J.C. Jaeger, *Proc. R. Soc. NSW*, 1942, vol. 76, 203-224
- [12] H.S. Carslaw, J.C. Jaeger, *Conduction of Heat in Solids*, 2nd ed., Oxford University Press, Oxford, United Kingdom, 1959
- [13] S.M. Kelly, Thermal and microstructure modeling of metal deposition processes with application to Ti-6Al-4V, Ph.D. thesis, Virginia Polytechnic Institute and State University, 2004.
- [14] Todd E. Sparks, Zhiqiang Fan, Measurement of laser absorption coefficient of several alloys for diode laser, unpublished report, 2006.
- [15] K. C. Mills, *Recommended values of thermophysical properties for selected commercial alloys*, Woodhead, Cambridge, 2002.
- [16] Tobias Lips, Bent Fritsche, A comparison of commonly used re-entry analysis tools, *Acta Astronautica* 57 (2005) 312-323.
- [17] F. Liou, J. Choi, R. Landers, V. Janardhan, S. Balakrishnan, S. Agarwal, *Proc. 12th Annual Solid Freeform Fabrication Symp.*, Austin, TX, Aug. 6–8, 2001, pp. 138-45.
- [18] M. Boddu, S. Musti, R. Landers, S. Agarwal, F. Liou, *Proc. 12th Annual Solid Freeform Fabrication Symp.*, Austin, TX, Aug. 6–8, 2001, pp. 452-59.

III. THREE-DIMENSIONAL MODELING OF HEAT TRANSFER AND FLUID FLOW IN LASER METAL DEPOSITION BY POWER INJECTION

ABSTRACT

A self-consistent three-dimensional model was developed for the laser metal deposition process by powder injection, which simulates heat transfer, phase changes, and fluid flow in the melt pool. The continuum model was adopted to deal with different phases in the calculation domain. The Piecewise Linear Interface Calculation (PLIC) method was implemented to track the free surface movement of the melt pool. Surface tension was modeled by taking the Continuum Surface Force (CSF) model combined with a force-balance flow algorithm. A laser-powder interaction model was developed to account for the effects of laser power attenuation and powder temperature rise during the laser metal deposition process. Temperature-dependent thermal-physical material properties were considered in the numerical implementation. The numerical model was validated by comparing simulations with experimental measurements.

1. INTRODUCTION

Laser metal deposition is an additive manufacturing technique which allows quick fabrication of fully-dense metallic components directly from Computer Aided Design (CAD) solid models. The applications include rapid prototyping, rapid tooling and part refurbishment. Laser metal deposition has an important advantage for these applications

because it can produce near-net shape parts with little or no machining [1]. In this paper the laser metal deposition process by powder injection is studied. As shown in Figure 1, laser deposition uses a focused laser beam as a heat source to create a melt pool on an underlying substrate. Powder material is then injected into the melt pool through nozzles. The incoming powder is metallurgically bonded with the substrate upon solidification. The part is fabricated in a layer by layer manner in a shape that is dictated by the CAD solid model. Laser metal deposition is characterized by small melt pool size, rapid changes of temperature and very short duration of the process. These characteristics make physical measurements of important parameters such as temperature and velocity fields, solidification rate and thermal cycles during laser metal deposition very difficult. These parameters are important because the melt pool convection patterns and the heating and cooling rates determine the geometry, composition, structure and the resulting properties of the deposit. For example, the buoyancy-driven flow due to temperature and species gradients in the melt pool strongly influences the microstructure and thus the mechanical properties of the final products. The surface tension-driven free-surface flow determines the shape and smoothness of the deposit.

Laser metal deposition involves many process parameters, including total power and power intensity distribution of the energy source, travel speed, translation path, material feed rate and shielding gas pressure. Physical phenomena associated with laser deposition processes are complex, including melting/solidification and vaporization phase changes, free-surface flow with surface tension, heat and mass transfer, and moving heat source, and laser metal interaction.

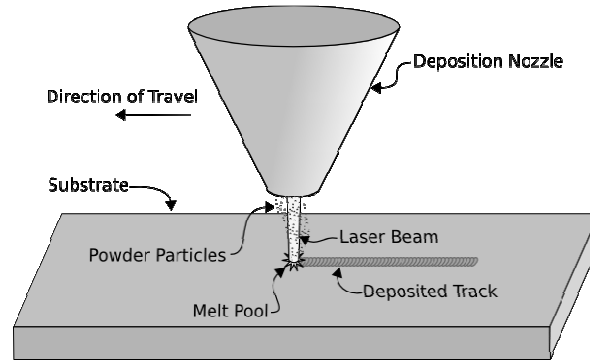


Figure 1. Schematics of a Coaxial Laser Metal Deposition System by Powder Injection

In recent decades, numerical calculations of heat transfer and fluid flow have been utilized to understand the evolution of temperature and velocity fields, and deposit geometry in laser metal deposition. Due to the physical complexity of the involved physical phenomena, the early models have been developed in a simplified way, e.g., neglecting the fluid motion in the molten pool or using predefined deposit geometry. Kar and Mazumder [2] solved analytically the one-dimensional heat and mass transfer equations for binary systems. The goal was to calculate the composition of the extended solid solution formed by rapid cooling. Weerasinghe and Steen [3] used a 3-D finite difference model to calculate the heat flux in the process. They took into account effects such as the particle cloud attenuation, heat absorption of the particles, and overlapping of the tracks. Hoadley and Rappaz [4] used a 2-D finite element model for the calculation of the quasi-steady state temperature field. They studied the influence of processing

parameters such as laser power and processing speed on dilution and clad thickness. Picasso et al. [5] used a 3-D analytical model for temperature to obtain process parameters such as travel speed and powder feed rate as a function of laser power, beam spot size, powder jet geometry and deposit height. The particle cloud attenuation effect and the dependence of the absorption coefficient on the angle of incidence of laser radiation into the melt pool were also considered. Kumar et al. developed a 3-D conduction heat transfer model [6] to predict the thermal behavior during laser deposition. Toyserkani et al. [7] developed a three-dimensional transient finite-element model for laser cladding with powder injection. They decoupled the interaction between the powder and melt pool to simplify the thermal analysis, and used a modified thermal conductivity to take into account the thermocapillary phenomena in the melt pool without calculating the fluid flow.

In order to simulate direct metal deposition process better, convection was incorporated into more and more models. Picasso and Rappaz [8] established a finite-element model to compute the shape of the melt pool. Their model took into account the interactions among the powder particles, and analyzed the effect of the laser beam properties and the change of absorption on the shape of the melt pool. Han et al. [9] presented a two-dimensional mathematical model for the laser deposition process, considering the powder injection effect on melt pool flow pattern and penetration. Interactions between laser, substrate, and powder as well as powder-substrate interactions have also been implemented. He and Mazumder [10] developed a 3-D model for direct metal deposition with coaxial powder injection. They used the level set method to track the free surface in the melt pool. None of the above publications used temperature dependent material properties. The material properties only differ from solid to liquid state.

In this study, a three-dimensional numerical model was developed for direct metal deposition with coaxial powder injection. Physical phenomena including heat transfer, melting and solidification phase changes, mass addition, and fluid flow in the melt pool were considered. Interactions between the laser beam and the coaxial powder flow, including the attenuation of beam intensity and temperature rise of powder particles before reaching the melt pool, were modeled. The volume of fluid method was implemented to precisely track the free surface movement of the melt pool. Temperature dependent material properties were implemented. The temperature and velocity fields, liquid/gas interface, and energy distribution at liquid/gas interface at different times were simulated.

2. MATHEMATICAL FORMULATION

2.1 Governing Equations. In this study, the calculation domain for a laser deposition system includes the substrate, melt pool, remelted zone, deposited layer and part of the gas region, as shown in Figure 2. The interface of solid and liquid phases in a multiconstituent alloying system can be morphologically very complex and forms a mushy zone that contains a mixture of both phases. In this study, the solid and liquid phases were treated as a continuum media, where the mushy region is modeled as a porous media. The continuum model [11, 12] was adopted to derive the governing equations in a binary solid/liquid phase change system. Some important terms for the melt pool, including the buoyancy force term and surface tension force term, have been added in the momentum equations. The molten metal was assumed to be Newtonian

fluid, and the melt pool was assumed to be an incompressible, laminar flow. The solid and liquid phases in the mushy zone were assumed to be in local thermal equilibrium.

The following equations were solved with appropriate boundary conditions.

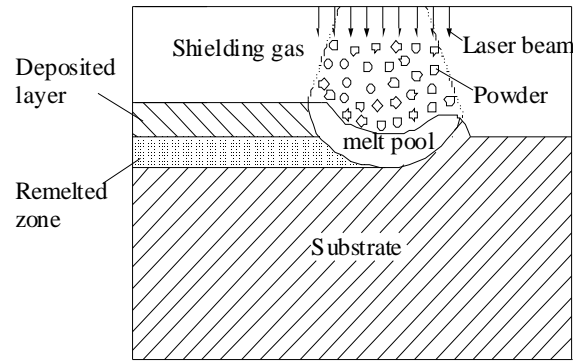


Figure 2. Schematic Diagram of the Calculation Domain for a Laser Deposition Process by Powder Injection

Mass conservation:

$$\frac{\partial \rho}{\partial t} + \nabla \cdot (\rho \mathbf{V}) = 0 \quad (1)$$

Momentum conservation:

$$\frac{\partial}{\partial t}(\rho u) + \nabla \cdot (\rho \mathbf{V}u) = \nabla \cdot \left(\mu_l \frac{\rho}{\rho_l} \nabla u \right) - \frac{\partial p}{\partial x} - \frac{\mu_l}{K} \frac{\rho}{\rho_l} (u - u_s) + \rho \mathbf{g}_x [1 - \alpha(T - T_0)] + \mathbf{F}_{Sx} \quad (2)$$

$$\frac{\partial}{\partial t}(\rho v) + \nabla \cdot (\rho \mathbf{V}v) = \nabla \cdot \left(\mu_l \frac{\rho}{\rho_l} \nabla v \right) - \frac{\partial p}{\partial y} - \frac{\mu_l}{K} \frac{\rho}{\rho_l} (v - v_s) + \rho \mathbf{g}_y [1 - \alpha(T - T_0)] + \mathbf{F}_{Sy} \quad (3)$$

$$\frac{\partial}{\partial t}(\rho w) + \nabla \cdot (\rho \mathbf{V}w) = \nabla \cdot \left(\mu_l \frac{\rho}{\rho_l} \nabla w \right) - \frac{\partial p}{\partial z} - \frac{\mu_l}{K} \frac{\rho}{\rho_l} (w - w_s) + \rho \mathbf{g}_z [1 - \alpha(T - T_0)] + \mathbf{F}_{Sz} \quad (4)$$

Energy conservation:

$$\frac{\partial}{\partial t}(\rho h) + \nabla \cdot (\rho \mathbf{V}h) = \nabla \cdot (k \nabla T) - \nabla \cdot [\rho (h_l - h)(\mathbf{V} - \mathbf{V}_s)] \quad (5)$$

where ρ is the density, t is the time, \mathbf{V} is the velocity vector, u , v , and w are the velocity components along the x , y , and z directions, respectively, μ is the viscosity, p is the pressure, \mathbf{g} is the gravity force vector, α is the thermal expansion coefficient, h is the enthalpy, T is the temperature, and k is the thermal conductivity. The subscripts s and l denote solid phase and liquid phase, respectively. Defining mass fraction f and volume fraction g , the density ρ , velocity \mathbf{V} , enthalpy h , and thermal conductivity k for a mixture of liquid and solid phases are

$$\rho = g_s \rho_s + g_l \rho_l \quad (6)$$

$$\mathbf{V} = f_s \mathbf{V}_s + f_l \mathbf{V}_l \quad (7)$$

$$h = f_s h_s + f_l h_l \quad (8)$$

$$k = g_s k_s + g_l k_l \quad (9)$$

where f_s and f_l refer to mass fractions of solid and liquid phases, and g_s and g_l are volume fractions of solid and liquid phases. To calculate these four quantities, g_l was calculated first and then the other three quantities were obtained according to the following relationships:

$$f_l = \frac{g_l \rho_l}{\rho} \quad f_s = \frac{g_s \rho_s}{\rho} \quad g_s + g_l = 1 \quad f_s + f_l = 1 \quad (10)$$

Supplementary relationships are required to update the volume fraction of liquid g_l during the melting/solidification process. For the target material Ti-6Al-4V, it was assumed that g_l is only dependent on temperature. The $g_l(T)$ function is given by [13]:

$$g_l = \begin{cases} 0 & \text{if } T < T_s \\ \frac{T - T_s}{T_l - T_s} & \text{if } T_s \leq T \leq T_l \\ 1 & \text{if } T > T_l \end{cases} \quad (11)$$

where T_s is the solidus temperature, and T_l is the liquidus temperature. The phase enthalpy for the solid and the liquid can be expressed as:

$$h_s = \int_0^T C_{ps}(T)dT \quad (12)$$

$$h_l = \int_0^{T_s} C_{ps}(T)dT + \int_{T_s}^T C_{pl}(T)dT + L_m \quad (13)$$

where L_m is the latent heat of melting. C_{ps} and C_{pl} are specific heat of solid and liquid phases, respectively.

In Eqs. (2) - (4), the third terms on the right-hand side are Darcy terms, representing the drag force when fluid passes through a porous media (dendrite structures). The isotropic permeability K is assumed to vary with liquid volume fraction according to the Kozeny-Carman equation [14]:

$$K = \frac{g_l^3}{C(1-g_l)^2} \quad (14)$$

where the parameter C is a constant depending on the morphology and size of the dendrites in the mushy zone. $K \rightarrow 0$ corresponds to a complete solid phase and $K \rightarrow \infty$ corresponds to a complete liquid phase. The fourth terms on the right-hand side of Eqs. (2) - (4) are the buoyancy force components due to temperature gradients. Here Boussinesq approximation is applied. T_0 is the reference temperature. The fifth terms on

the right-hand side of Eqs. (2) - (4) are surface tension force components, which will be described in Section C.

2.2 Free Surface Tracking. In laser metal deposition by power injection, the metal pool is free to deform due to powder impingement, surface tension and other forces. The evolution of the free surface of melt pool determines the quality of solidified geometry and surface roughness of the deposit layer. Geometries of the free surface determine the surface capillary and thermocapillary forces, and thus the fluid flow in the melt pool. In addition, an accurate interface reconstruction enables the calculation of the incident angle of the laser beam. In this study the Volume of Fluid (VOF) method [15] was adopted to track the evolution of the free surface in the melt pool. In this method a scalar indicator function, F , is defined on the grid to indicate the liquid-volume fraction in each computational cell. Volume fraction values between zero and unity indicate the presence of the interface. VOF has been adopted by many in-house codes and built into commercial codes (SOLA-VOF [16], NASA-VOF2D [17], NASA-VOF3D [18], RIPPLE [19], and FLOW3D [20], ANSYS Fluent, to name a few). The Volume of Fluid function, F , satisfies the following conservation equation:

$$\frac{\partial F}{\partial t} + (\mathbf{V} \cdot \nabla) F = 0 \quad (15)$$

The VOF method consists of an interface reconstruction algorithm and a volume fraction advection scheme. The features of these two steps are used to distinguish different VOF versions. In this study the Piecewise Linear Interface Calculation (PLIC) scheme [21-23], which approximates the interface as a plane within a computational cell, was used to

solve Equation (15). Compared to earlier versions of the VOF methods [15, 24-26], PLIC-VOF is more accurate and avoids the numerical instability [27]. It also allows dealing with large deformation of the interface.

In the PLIC, at each time step, given the volume fraction in each computational cell and an estimate of the normal vector to the interface, the interface in each cell is represented by a plane portion (intersection of a plane with the computational cell). This planar interface is then propagated by the flow and the resulting volume, mass, momentum, and heat fluxes into neighboring cells are determined. In a 3D calculation, a reconstructed planar surface satisfies the following equation:

$$n_x x + n_y y + n_z z = d \quad (16)$$

where n_x , n_y and n_z are x , y and z components of the interface normal vector, respectively. d is a parameter related to the distance between the plane surface and the coordinate origin of the reference cell. In the interface reconstruction step, n_x , n_y and n_z of each cell are calculated based on volume fraction data, using a three steps procedure as described in [28]. Then the parameter d is determined to match the given volume fraction. Finally given the velocity field, the reconstructed interface is advected according to the combined Eulerian-Lagrangian scheme in [28].

2.3 Surface Tension. The surface tension force, F_S , is given by:

$$\mathbf{F}_S = \gamma \kappa \hat{\mathbf{n}} + \nabla_s \gamma \quad (17)$$

where γ is surface tension coefficient, κ is the curvature of the interface, $\hat{\mathbf{n}}$ is the unit normal to the local surface, and ∇_s is the surface gradient operator. The term $\gamma\kappa\hat{\mathbf{n}}$ is the normal component of the surface tension force. The term $\nabla_s\gamma$ represents the Marangoni effect caused by spatial variations in the surface tension coefficient along the interface due to temperature and/or species gradients. It causes the fluid flow from regions of lower to higher surface tension coefficient.

In this study, surface tension was modelled as a volume force using the Continuum Surface Force (CSF) model [29], combined with a force-balance flow algorithm [30]. The basic idea underlying the CSF model is the representation of surface tension as a continuous force per unit volume that acts in a finite transition region between the liquid and gas phases. As shown in Figure 3, the liquid-gas interface (the free surface) is modeled as a transition region of thickness h across which the density varies from its liquid value to gas value. By the CSF formulation, discontinuities can be approximated without increasing the overall error of approximation. The transition thickness is a length comparable to the resolution of the computational mesh.

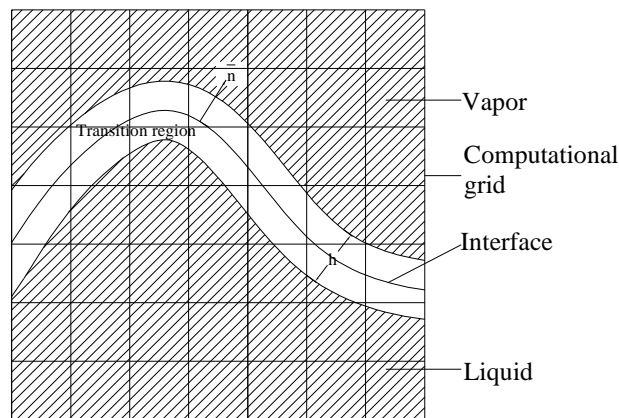


Figure 3. CSF Representation of a Liquid/Gas Interface

Interface normals are calculated based on the three steps procedure as described in [28]. The interface curvature, κ , was calculated using the height function (HF) technique. For an interfacial cell, (i, j, k) , in which the absolute value of the z component of the interface normal vector, \mathbf{n} , is largest, height functions are constructed by integrating volume fractions in the z -direction as

$$H_{i,j,k} = \sum_{t=-t_{down}}^{t_{up}} F_{i,j,k+t}^* \Delta z \quad (18)$$

where t_{down} and t_{up} are adaptively adjusted from 1 to 3 depending on the local grid resolution, Δz is the mesh size in z -direction and F^* is a modified distribution of the volume fraction, F , which is forced to follow a local monotonic variation along the z direction. The curvature of the interface is determined from the height function H as

$$\kappa = \frac{H_{xx} + H_{yy} + H_{xx}H_y^2 + H_{yy}H_x^2 - 2H_{xy}H_xH_y}{(1 + H_x^2 + H_y^2)^{3/2}} \quad (19)$$

where the partial derivatives of H are obtained using the finite difference formula proposed by López et al. [31], which considerably improves the curvature accuracy in three-dimensional problems. For example, the derivatives H_x and H_{xx} (as in the y -direction) are obtained as [31]

$$H_{x(i,j,k)} = \frac{\gamma(H_{i+1,j+1,k} - H_{i-1,j+1,k}) + H_{i+1,j,k} - H_{i-1,j,k} + \gamma(H_{i+1,j-1,k} - H_{i-1,j-1,k})}{2\Delta z(1 + 2\gamma)} \quad (20)$$

$$H_{xy(i,j,k)} = \frac{\gamma(H_{i+1,j+1,k} - 2H_{i,j+1,k} + H_{i-1,j+1,k}) + H_{i+1,j,k} - 2H_{i,j,k} + H_{i-1,j,k} + \gamma(H_{i+1,j-1,k} - 2H_{i,j-1,k} + H_{i-1,j-1,k})}{\Delta z^2(1 + 2\gamma)} \quad (21)$$

where the parameter γ is defined as

$$\gamma = \begin{cases} 0.0 & \text{if } \theta = \arccos[\max(|n_x|, |n_y|, |n_z|)] < 0.8 \text{ rad} \\ 0.2 & \text{otherwise} \end{cases} \quad (22)$$

The cross derivative H_{xy} is calculated as

$$H_{xy(i,j,k)} = (H_{i+1,j+1,k} - H_{i+1,j-1,k} - H_{i-1,j+1,k} + H_{i-1,j-1,k}) / (4\Delta z^2) \quad (23)$$

2.4 Laser-Powder Interaction. It has been verified experimentally that the spatial concentration profile of a converged coaxial powder flow can be considered as a Gaussian distribution [32] as defined in the following equation:

$$C(r,l) = C_{peak}(l) \exp\left(-\frac{2r^2}{R_p^2}\right) \quad (24)$$

where C is the powder concentration (the number of powder particles per unit volume), which is a function of radial r and axial distances l in an axial-symmetrical coordinate, C_{peak} is the powder concentration at the center of powder flow ($r = 0$), and R_p is the effective radius of powder stream at position l . Powder particles are heated by the laser beam and experience temperature rise and even phase changes before reaching the

substrate. Meanwhile, the laser beam is attenuated by absorption, reflection, and scattering effects of the particle cloud. The amount of attenuated laser power resulting from the powder cloud shadow primarily depends on the particle travel distance, particle injection velocity, particle material properties, and mass flow rate. Based on the experimental investigation, Frenk et al. [33] suggested a practical equation to calculate the attenuated power in the situation of the side nozzle, which can be rewritten for the coaxial case as

$$P_{atten} = P_{laser} \left[1 - \exp \left(- \frac{3Q_{ext} \dot{m} L}{\pi \rho r_p D_{jet} v_p} \right) \right] \quad (25)$$

where P_{laser} is the power of laser beam, \dot{m} denotes the powder mass flow rate, L is the stand-off distance from the nozzle exit to the substrate, ρ is powder density, r_p is the radius of the powder particle, D_{jet} is the diameter of the powder jet, v_p is the powder injection velocity, and Q_{ext} is the extinction coefficient. It is assumed that the extinction cross section is close to the actual geometrical cross section, and Q_{ext} takes a value of unity. Particle temperature was calculated taking a simplified model proposed by Jouvard et al. [34], which is in good agreement with the experiment. In this model the increased enthalpy acquired by each particle is given by

$$dh_p = \frac{S_p}{S} \eta P_i(z) \frac{dz}{v_p} \quad (26)$$

where S_p is the cross-sectional area of the particle, S is the section area of collimated laser beam, v_p is the particle velocity, η is the laser absorption coefficient, and P_t is the laser power transmitted through the powder cloud. In Jouvard's model P_t was assumed to be equal to the initial laser power. Here, it was quantified as the difference between incident laser power, P_{laser} , and attenuated laser power, P_{atten} . Once the increased enthalpy was solved by integrating Eq. (26) numerically, the particle temperature at its impinging time can be derived using enthalpy transformation that considers the latent heat of melting. The laser absorption coefficient η as a function of temperature is related to the substrate resistivity and the wavelength of the laser radiation by the following relation [35]:

$$\eta(T) = 0.365\left(\frac{\beta}{\lambda}\right)^{1/2} - 0.0667\left(\frac{\beta}{\lambda}\right) + 0.006\left(\frac{\beta}{\lambda}\right)^{3/2} \quad (27)$$

where β is the electrical resistivity of the material in Ω cm, and λ is the wavelength in cm. For the diode laser in this study and a substrate of Ti-6Al-4V, the laser absorption coefficient used in the calculation was 0.4.

2.5 Boundary Conditions. Energy balance at the free surface satisfies the following equation:

$$k \frac{\partial T}{\partial \mathbf{n}} = \frac{\eta(P_{laser} - P_{atten})}{\pi R^2} - h_c(T - T_\infty) - \varepsilon\sigma(T^4 - T_\infty^4) - \dot{m}_e L_v \quad (28)$$

where terms on the right-hand side are laser irradiation, convective heat loss, radiation heat loss and evaporation heat loss, respectively. R is the radius of laser beam spot, η is

the laser absorption coefficient, \dot{m}_e is the evaporation mass flux, L_v is the latent heat of evaporation, h_c is the heat convective coefficient, ε is the emissivity, σ is the Stefan-Boltzmann constant, and \mathbf{n} is the normal vector at the local interface. \dot{m}_e can be evaluated according to the “overall evaporation model” in [36]. \dot{m}_e is of the form:

$$\log \dot{m}_e = A + \log p_0 - 0.5 \log T \quad (29)$$

where A is a constant dependent on the material, and p_0 is the vapor pressure.

On the bottom surface and side surfaces, energy boundary conditions are given by

$$k \frac{\partial T}{\partial \mathbf{n}} + h_c (T - T_\infty) = 0 \quad (30)$$

The boundary conditions for Eqs. (2) – (4) at the free surface in the melt pool include velocity continuity and stress balance. The velocity continuity conditions are given by:

$$\mathbf{V}_1 \cdot \mathbf{n} = \mathbf{V}_2 \cdot \mathbf{n} \quad (31)$$

$$\mathbf{V}_1 \cdot \mathbf{t} = \mathbf{V}_2 \cdot \mathbf{t} \quad (32)$$

where \mathbf{n} and \mathbf{t} are the unit normal vector and unit tangent vector to the local interface, respectively. Subscripts 1 and 2 denote the liquid phase and the gas phase, respectively.

The stress balance at the free surface is given by

$$(\boldsymbol{\sigma}_1 - \boldsymbol{\sigma}_2) \cdot \mathbf{n} = \kappa\gamma\mathbf{n} \quad (33)$$

where $\boldsymbol{\sigma}_1$ and $\boldsymbol{\sigma}_2$ represent the stress tensors in each fluid. In this study one fluid in a vacuum was considered, thus $\boldsymbol{\sigma}_2 = 0$. After some math manipulations, the following relationships derived from Eq. (33) are obtained:

Normal direction:

$$\begin{aligned} -p + 2\mu[n_x n_x \frac{\partial u}{\partial x} + n_y n_y \frac{\partial v}{\partial y} + n_z n_z \frac{\partial w}{\partial z} + n_x n_y (\frac{\partial u}{\partial y} + \frac{\partial v}{\partial x}) + n_x n_z (\frac{\partial u}{\partial z} + \frac{\partial w}{\partial x}) \\ + n_y n_z (\frac{\partial v}{\partial z} + \frac{\partial w}{\partial y})] = \kappa\gamma \end{aligned} \quad (34)$$

Tangential direction 1:

$$\begin{aligned} 2n_x l_x \frac{\partial u}{\partial x} + 2n_y l_y \frac{\partial v}{\partial y} + 2n_z l_z \frac{\partial w}{\partial z} + (n_x l_y + n_y l_x) (\frac{\partial u}{\partial y} + \frac{\partial v}{\partial x}) \\ + (n_x l_z + n_z l_x) (\frac{\partial u}{\partial z} + \frac{\partial w}{\partial x}) + (n_y l_z + n_z l_y) (\frac{\partial v}{\partial z} + \frac{\partial w}{\partial y}) = 0 \end{aligned} \quad (35)$$

Tangential direction 2:

$$\begin{aligned} 2n_x m_x \frac{\partial u}{\partial x} + 2n_y m_y \frac{\partial v}{\partial y} + 2n_z m_z \frac{\partial w}{\partial z} + (n_x m_y + n_y m_x) (\frac{\partial u}{\partial y} + \frac{\partial v}{\partial x}) \\ + (n_x m_z + n_z m_x) (\frac{\partial u}{\partial z} + \frac{\partial w}{\partial x}) + (n_y m_z + n_z m_y) (\frac{\partial v}{\partial z} + \frac{\partial w}{\partial y}) = 0 \end{aligned} \quad (36)$$

where (n_x, n_y, n_z) is the unit normal vector, and (l_x, l_y, l_z) and (m_x, m_y, m_z) are the unit tangential vectors. In the VOF framework, application of tangential stress conditions means that we seek to let some of the normal/tangential components equal to zero. On the bottom surface and side surfaces, velocity boundary conditions are given by

$$\mathbf{V} = 0 \quad (37)$$

2.6 Numerical Implementation. A typical calculation domain used in this study was $10 \times 10 \times 5$ mm in x , y , and z direction, with a grid of $500 \times 500 \times 250$. Discretization of the governing equations was carried out in the physical space using the finite volume method. A forward staggered, fixed grid was used, in which scalar quantities are located at the geometric center of the cell, whereas velocity components lie at the cell face centers. For discretization of the advection terms, the flux limiter scheme MUSCL (stands for Monotone Upstream-centered Schemes for Conservation Laws) [37] was applied to improve the accuracy of the upstream approximation and enforce the weak monotonicity in the advected quantity. The computational cycle can be described through the following iterative steps:

- 1) Equations (1) - (4) and the related boundary conditions are solved iteratively using a two-step projection method [38] to obtain velocities and pressures. The second step of the two-step projection method [38] requires a solution of a Poisson equation for the pressure field,

$$\nabla \cdot \left[\frac{1}{\rho^n} \nabla p^{n+1} \right] = \frac{\nabla \cdot \tilde{\mathbf{V}}}{\delta t} \quad (38)$$

where ρ^n is the density from the old time step, p^{n+1} is the pressure to be solved at the new time step, and $\tilde{\mathbf{V}}$ is the temporary velocity field computed from the first step.

The density retained inside the divergence operator in Eq. (38) results in an extra term proportional to $\nabla \rho$, which contributes to the pressure solution within the free surface transition region where $\nabla \rho \neq 0$. The system of linear equations formulated from the finite volume approximation of Eq. (38) was solved with an ICCG (Incomplete Cholesky Conjugate Gradient) solution technique [39]. Thermo-physical properties used in this step are computed from the old temperature field.

- 2) Equation (5) is solved by a method [40] based on a finite volume discretization of the enthalpy formulation of Equation (4). Once new temperature field is obtained, the thermo-physical properties are updated.
- 3) Equation (15) is solved using the PLIC-VOF [21-23] to obtain the updated free surface, geometry of the melt pool and thermal field.
- 4) Advance to the next time step and back to step 1 until the desired process time is reached.

The time step is taken at the level of 10^{-6} s initially and adapted subsequently according to the convergence and stability requirements of the Courant–Friedrichs–Lewy (CFL) condition, the explicit differencing of the Newtonian viscous stress tensor, the explicit treatment of the surface tension force, and heat conduction. The time step constraint due to convection (the CFL condition) is given by

$$\delta t < \min \left\{ \frac{\delta x_i}{|u_{i,j,k}|}, \frac{\delta y_j}{|v_{i,j,k}|}, \frac{\delta z_k}{|w_{i,j,k}|} \right\} \quad (39)$$

The time step constraint due to viscosity requires

$$\delta t < \frac{1}{2\nu} (\delta x_i^{-2} + \delta y_j^{-2} + \delta z_k^{-2})^{-1} \quad (40)$$

The explicit treatment of the surface tension force requires that capillary waves not travel more than one cell width in one step. A rough estimate for this limit is

$$\delta t < \left(\frac{\rho h^3}{2\pi\gamma} \right)^{1/2} \quad (41)$$

Time step constraint due to heat conduction is

$$\delta t < \frac{1}{6} \frac{h^2}{D} \quad (42)$$

In the above Equations. (39) – (42), δx_i , δy_j , and δz_k are the width of the cell (i, j, k) in x -, y - and z -directions, respectively. $u_{i,j,k}$, $v_{i,j,k}$ and $w_{i,j,k}$ are x , y and z components of

the velocity vector in cell (i, j, k) , respectively. ν is the kinematic viscosity of the liquid metal. D is the thermal diffusivity of the material. The minimum function was taken over every cell in the mesh. h is the minimum of δx_i , δy_j , and δz_k .

In this study, laser deposition processes by the LAMP deposition system of Missouri S&T with a 1000 W diode laser were modeled. The laser emits at 808 nm and operates in the continuous wave (CW) mode. The parameters for the simulation were chosen based on the capability of our experimental facilities to compare the simulation results with the experimental measurements. The main properties of material Ti-6Al-4V are listed in Table 1.

3. RESULTS AND DISCUSSION

A predicted 3D track of the process is illustrated in Figure 4. As seen in Figure 4, a melt pool is generated at the front of the track with the moving laser beam. The laser energy affects a small zone and does not degrade the material elsewhere. It can be seen that the intense heat causes substrate melting, which generates a good bond between the track and base material. To better examine the fluid motion in the melt pool and mushy zone, the velocity field is separately shown in Figure 5. As seen in Figure 5, the fluid velocity decreases when the melt flows through the mushy zone where a damping effect in a porous media occurs.

To compare with the numerical results, the same process parameters were used in a deposit experiment. The deposit heights and widths are compared between simulated and experimental results as shown in Figures 6–7. The trends of the calculated values

Table 1. Main Material Properties for Powder and Substrate

Property, symbol (unit)	Value	Reference
Liquidus temperature, T_l (K)	1923.0	[41]
Solidus temperature, T_s (K)	1877.0	[42]
Evaporation temperature, T_v (K)	3533.0	[42]
Solid specific heat, C_{ps} ($J kg^{-1} K^{-1}$)	$\begin{cases} 483.04 + 0.215T & T \leq 1268K \\ 412.7 + 0.1801T & 1268 < T \leq 1923 \end{cases}$	[41]
Liquid specific heat, C_{pl} ($J kg^{-1} K^{-1}$)	831.0	[41]
Thermal conductivity, k ($W m^{-1} K^{-1}$)	$\begin{cases} 1.2595 + 0.0157T & T \leq 1268K \\ 3.5127 + 0.0127T & 1268 < T \leq 1923 \\ -12.752 + 0.024T & T > 1923 \end{cases}$	[41]
Solid density, ρ_s ($kg m^{-3}$)	$4420 - 0.154 (T - 298 K)$	[41]
Liquid density, ρ_l ($kg m^{-3}$)	$3920 - 0.68 (T - 1923 K)$	[41]
Latent heat of melting, L_m ($J kg^{-1}$)	2.86×10^5	[41]
Latent heat of evaporation, L_v ($J kg^{-1}$)	9.83×10^6	[41]
Dynamic viscosity, μ ($N m^{-1} s^{-1}$)	3.25×10^{-3} (1923K), 3.03×10^{-3} (1973K), 2.66×10^{-3} (2073K), 2.36×10^{-3} (2173K)	[41]
Radiation emissivity, ε	$0.1536 + 1.8377 \times 10^{-4} (T - 300.0 K)$	[43]
Surface tension ($N m^{-1}$), γ	$1.525 - 0.28 \times 10^{-3} (T - 1941K)^a$	[41]
Thermal expansion coeff., α (K^{-1})	1.1×10^{-5}	[41]

^aValue for commercially pure titanium was used.

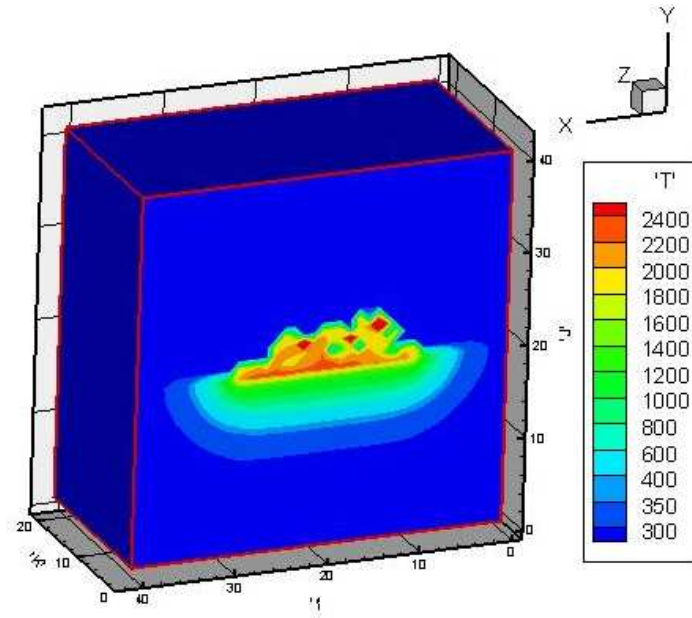


Figure 4. 3D Deposition Profile and Temperature Distribution
with Cross Section at $t = 0.11$ s

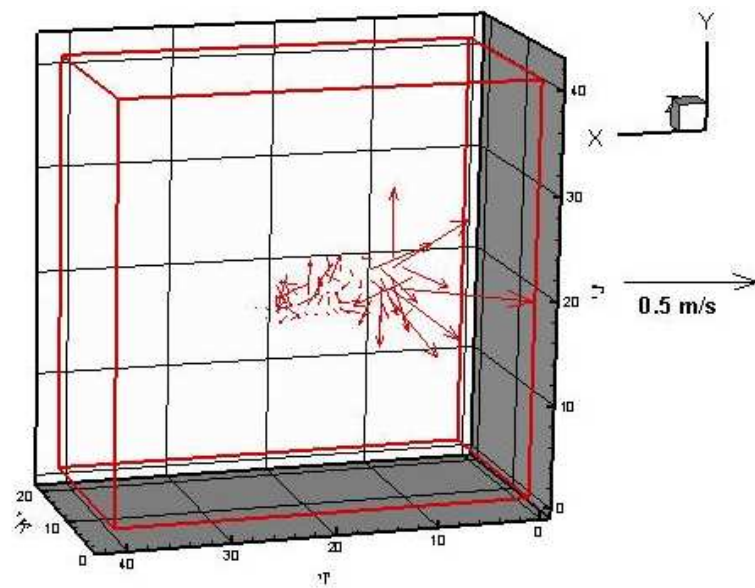


Figure 5. Fluid Velocity Fields in the Melt Pool in Cross Section
along the Laser Scanning Direction at $t = 0.11$ s

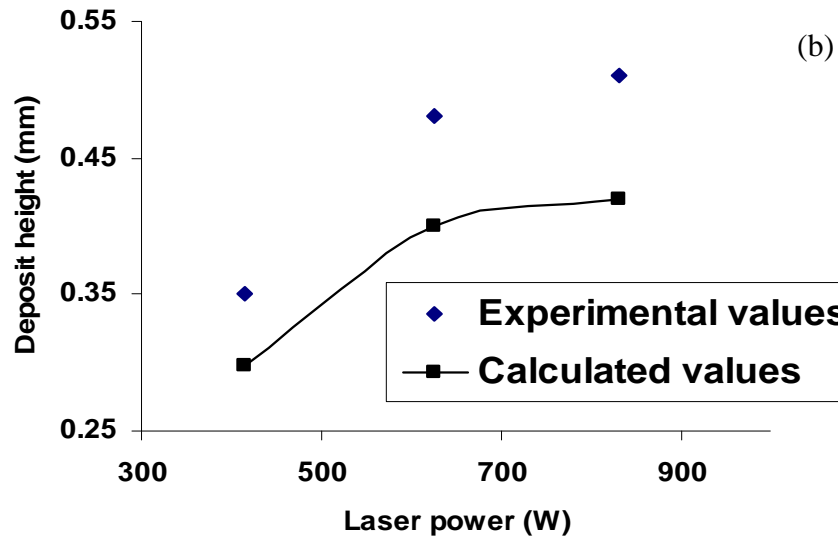
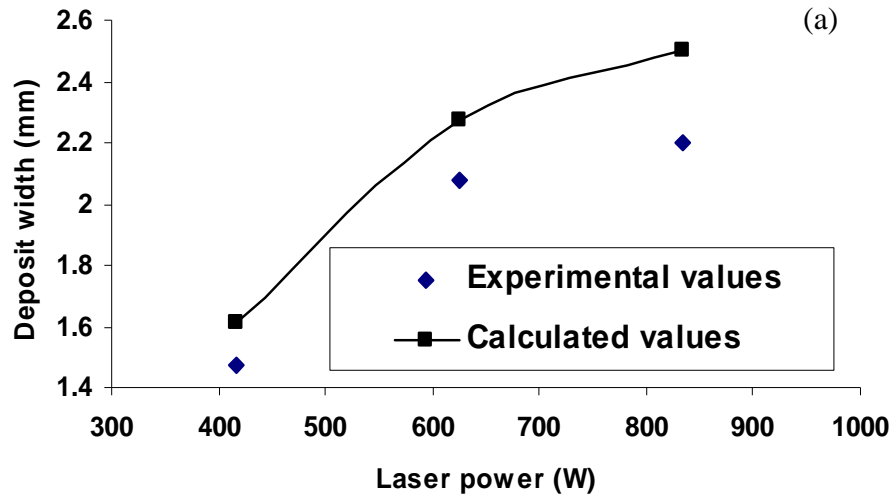


Figure 6. Comparison between Experimental and Calculated Deposit Width (a) and Deposit Height (b) at Different Laser Powers

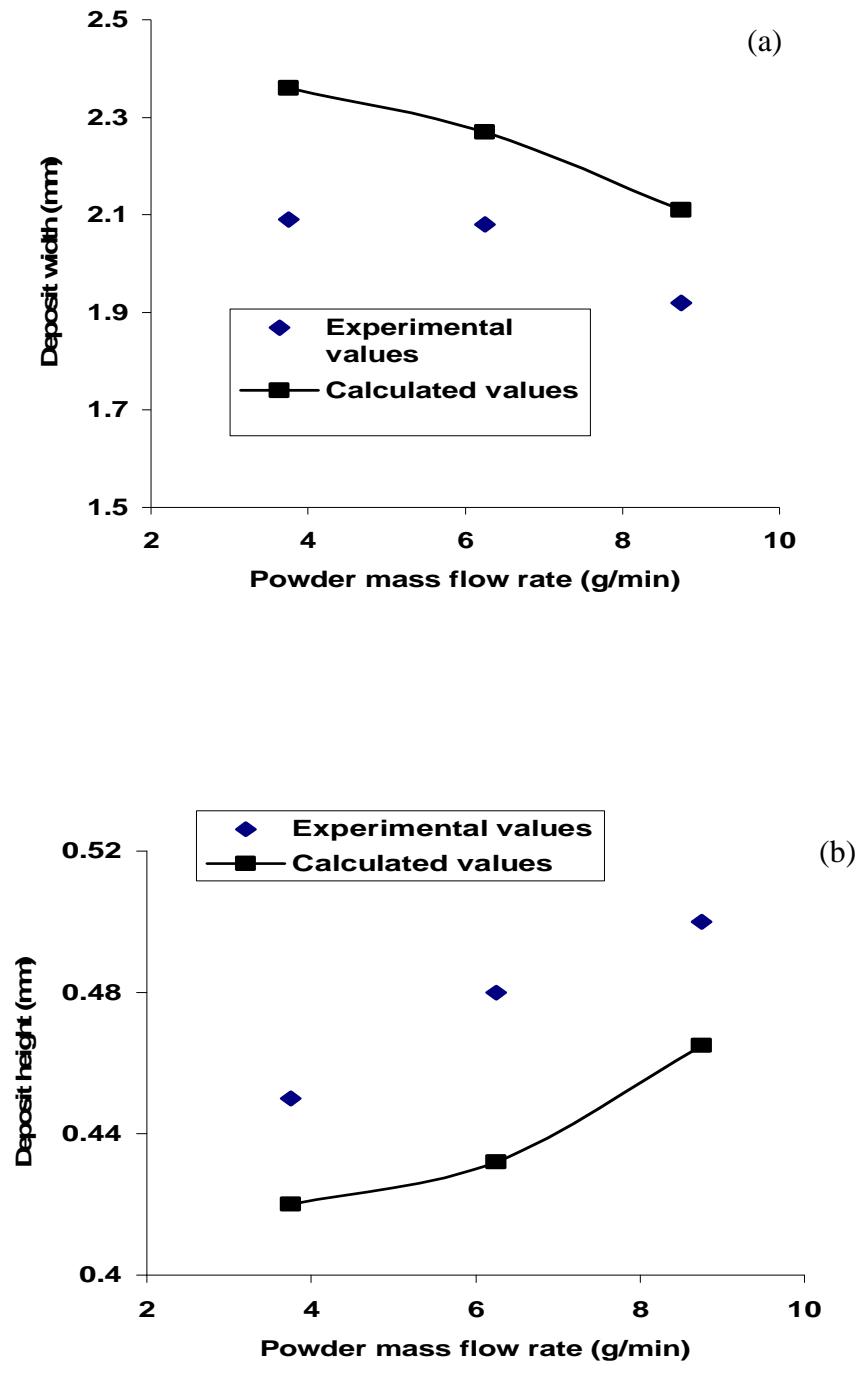


Figure 7. Comparison between Experimental and Calculated Deposit Width (a) and Deposit Height (b) at Different Powder Mass Flow Rates

reasonably match those of experimental results, thus validating the model. Higher laser power increases the deposit width and deposit height. A better agreement between experimental and calculated results can be obtained at lower laser power. The discrepancy at higher power may be mainly caused by the uncertainties for the temperature-dependent thermophysical data, such as thermal conductivity and specific heat. Higher powder mass flow rate decreases the deposit width but increase the deposit height. The fact that higher powder mass flow rate decreases the deposit width can be explained by the powder cloud attenuation effect. Higher powder flow rate means less energy available to be absorbed by the substrate to form the melt pool. For the calculation of deposit height, the difference between calculated and experimental results is potentially due to the variance of the powder concentration distribution in the real process from the assumed Gaussian distribution in the model.

4. CONCLUSIONS

A self-consistent three-dimensional model was developed for the laser metal deposition process by powder injection, which simulates heat transfer, phase changes, and fluid flow in the melt pool. Transport equations were solved with the finite volume method. Temperature and fluid velocity were solved in a coupled manner.

Physical phenomena at the liquid/gas and solid/liquid interfaces were successfully incorporated in the governing equations as boundary conditions, such as the thermocapillary and capillary forces at the liquid/gas interface in the momentum

equations, Stefan's conditions at the solid/liquid interface in the energy equation, and convection and radiation heat losses at the liquid/gas interface in the energy equation.

The continuum model was adopted to deal with different phases (gas, liquid, solid, and mushy zone) in the calculation domain. The Piecewise Linear Interface Calculation (PLIC) method was implemented to track the free surface movement of the melt pool due to the powder addition and fluid flow. A laser-powder interaction model was developed in this study to account for the effects of laser power attenuation and powder temperature rise during the laser metal deposition process. Simulated track heights and widths agree well with experimental ones. The model provides a means for optimizing the process parameters and controlling the process.

5. ACKNOWLEDGEMENTS

This research was supported by US National Aeronautics and Space Administration (NASA) Grant Number NNX11AI73A, Product Innovation and Engineering, LLC, and Missouri S&T Intelligent Systems Center and Material Research Center. Their support is greatly appreciated.

6. REFERENCES

1. F. Liou and M. Kinsella (2009), A Rapid Manufacturing Process for High Performance Precision Metal Parts. *Proceedings of RAPID 2009 Conference & Exposition, Society of Manufacturing Engineers, Schaumburg, IL, USA, May 2009.*

2. A. Kar and J. Mazumder (1988), One-dimensional finite-medium diffusion model for extended solid solution in laser cladding of Hf on nickel, *Acta Metall.*, 1988, vol. 36, pp. 701-12.
3. V.M. Weerasinghe and W.M. Steen (1983), in *Transport Phenomena in Materials Processing*, M. Chen, J. Mazumder, and C. Tucker, eds., ASME, New York, NY, 1983, pp. 15-23.
4. AFA Hoadley and M. Rappaz (1992), A Thermal Model of Laser Cladding by Powder Injection, *Metall. Trans. B*, 1992, vol. 23B, pp. 631-42.
5. M. Picasso, C. F. Marsden, J-D Wagniere, A. Frenk and M. Rappaz (1994), A simple but realistic model for laser cladding, *Metallurgical and Materials Transactions B*, Vol. 25B, (1994), pp.281-291..
6. S. Kumar, S. Roy, C. P. Paul, and A. K. Nath (2008), Three-dimensional conduction heat transfer model for laser cladding process, *Numer. Heat Transfer, Part B*, 2008, Vol.53, No.3, pp. 271-287.
7. E. Toyserkani, A. Khajepour, and S. Corbin (2002), A 3-D transient finite element model for laser cladding by powder injection, *Proceedings of ICALEO 2002*, Scottsdale, AZ, Oct. 14–17, 2002.
8. M. Picasso and M. Rappaz (1994), Laser-powder-material interactions in the laser cladding process, *J. Phys.*, 1994, vol. IV (C4), pp. 27-33.
9. L. Han, F. W. Liou, and K. M. Phatak (2004), Modeling of laser cladding with powder injection, *Metall. Mater. Trans. B*, 2004, vol. 35B, pp. 1139–50.
10. X. He and J. Mazumder (2007), Transport phenomena during direct metal deposition, *J. Appl. Phys.*, 2007, Vol. 101, 053113.
11. W. D. Bennon and F. P. Incropera(1987), A continuum model for momentum, heat and species transport in binary solid-liquid phase change systems-I. Model formulation, *International Journal of Heat and Mass Transfer*, Vol. 30, No. 10, (October 1987), pp.2161-2170, ISSN 0017-9310.
12. P.J. Prescott, F.P. Incropera, and W.D. Bennon(1991), Modeling of Dendritic Solidification Systems: Reassessment of the Continuum Momentum Equation. *International Journal of Heat and Mass Transfer*, Vol. 34, No. 9, (September 1991), pp. 2351-2360, ISSN 0017-9310.
13. C. R. Swaminathan and V. R. Voller (1992), A general enthalpy method for modeling solidification processes. *Metallurgical Transactions B*, Vol. 23, No. 5, (October 1992), pp. 651-664, ISSN 1073-5615.

14. P.C. Carman (1937), Fluid flow through granular beds. *Transactions of the Institution of Chemical Engineers*, Vol. 15, (February 1937), pp. 150-166, ISSN 0046-9858.
15. C.W. Hirt and B.D. Nichols (1981), Volume-of-fluid (VOF) for the dynamics of free boundaries. *Journal of Computational Physics*, Vol. 39, No.1, (January 1981), pp. 201-225, ISSN 0021-9991.
16. B. D. Nichols, C. W. Hirt and R. S. Hotchkiss (1980), *SOLA-VOF: A solution algorithm for transient fluid flow with multiple free boundaries*, Technical Report, LA-8355, Los Alamos National Lab.
17. M. D. Torrey, L. D. Cloutman, R. C. Mjolsness and C. W. Hirt (1985), *NASA-VOF2D: a computer program for incompressible flow with free surfaces*, Technical Report, LA-101612-MS, Los Alamos National Lab.
18. M. D. Torrey, R. C. Mjolsness and L. R. Stein (1987), *NASA-VOF3D: a three-dimensional computer program for incompressible flow with free surfaces*, Technical Report, LA-11009-MS, Los Alamos National Lab.
19. D. B. Kothe, R. C. Mjolsness, and M. D. Torrey (1991), *RIPPLE: A Computer Program for Incompressible Flows with Free surfaces*, Technical Report, LA-12007-MS, Los Alamos National Lab.
20. C. W. Hirt and B. D. Nichols (1988), *Flow-3D user manual*, Technical Report, Flow Sciences, Inc.
21. D. Gueyffier, J. Li, A. Nadim, R. Scardovelli and S. Zaleski (1999), Volume of Fluid interface tracking with smoothed surface stress methods for three-dimensional flows. *Journal of Computational Physics*, Vol. 152, No.2, (July 1999), pp. 423-456, ISSN 0021-9991.
22. R. Scardovelli and S. Zaleski (2000), Analytical relations connecting linear interfaces and volume fractions in rectangular grids, *Journal of Computational Physics*, Vol. 164, No.1, (October 2000), pp. 228-237, ISSN 0021-9991.
23. R. Scardovelli and S. Zaleski (2003), Interface Reconstruction with Least-Square Fit and Split Eulerian-Lagrangian Advection. *International Journal for Numerical Methods in Fluids*, Vol. 41, No.3, (January 2003), pp. 251-274, ISSN 0271-2091.
24. A.J. Chorin (1980), Flame advection and propagation algorithms, *Journal of Computational Physics*, Vol. 35, No. 1, (March 1980), pp. 1-11, ISSN 0021-9991.
25. R. Debar (1974), *Fundamentals of the KRAKEN Code*, Technical Report UCIR-760, Lawrence Livermore National Laboratory, 1974.
26. W.F. Noh and P.R. Woodward (1976), SLIC (simple line interface calculation), *Lecture Notes in Physics*, Vol. 59, pp. 330-340, ISSN 0075-8450.

27. R. Scardovelli and S. Zaleski (1999), Direct numerical simulation of free-surface and interfacial flow, *Annual Review of Fluid Mechanics*, Vol. 31, (January 1999), pp. 567-603, ISSN 0066-4189.
28. E. Aulisa, S. Manservigi, R. Scardovelli and S. Zaleski (2007), Interface reconstruction with least-squares fit and split advection in three-dimensional Cartesian geometry, *Journal of Computational Physics*, Vol. 225, No.2, (August 2007), pp. 2301-2319, ISSN 0021-9991.
29. J.U. Brackbill, D.B. Kothe and C. Zemach (1992), A continuum method for modeling surface tension, *Journal of Computational Physics*, Vol. 100, No.2, (June 1992), pp. 335-354, ISSN 0021-9991.
30. E. Shirani, N. Ashgriz and J. Mostaghimi (2005), Interface pressure calculation based on conservation of momentum for front capturing methods. *Journal of Computational Physics*, Vol. 203, No. 1, (February 2005), pp. 154-175, ISSN 0021-9991.
31. J. López and J. Hernández (2010), On reducing interface curvature computation errors in the height function technique, *Journal of Computational Physics*, Vol.229, No.13, (July 2010), pp. 4855-4868, ISSN 0021-9991.
32. Jehnming Lin (2000), Laser attenuation of the focused powder streams in coaxial laser cladding, *Journal of Laser Applications*, Vol. 12, No. 1, (February 2000), pp. 28-33.
33. A. Frenk, M. Vandyoussefi, J. Wagniere, A. Zryd and W. Kurz (1997), Analysis of the lasercladding process for stellite on steel, *Metallurgical and Materials Transactions B*, Vol.28, No.3, (June 1997), pp. 501-508, ISSN 1073-5615.
34. J.M. Jouvard, D.F. Grevey, F. Lemoine, and A.B. Vannes, Continuous wave Nd: YAG laser cladding modelling: a physical study of track creation during low power processing, *J. Laser Appl.*, 1997, vol. 9, pp. 43-50.
35. M. A. Bramson (1968), *Infrared Radiation: A Handbook for Applications*, Plenum, New York, 1968.
36. M. Choi, R. Greif and M. Salcudean (1987), A study of the heat transfer during arc welding with applications to pure metals or alloys and low or high boiling temperature materials, *Numerical Heat Transfer*, Vol. 11, No.4, (April 1987) pp. 477-491, ISSN 0149-5720.
37. B. van Leer (1979), Towards the Ultimate Conservative Difference Scheme, V. A Second Order Sequel to Godunov's Method, *J. Com. Phys.*, 32, 1979, pp. 101-136.
38. A.J. Chorin (1968), Numerical solution of the Navier-Stokes equations, *Mathematics of Computation*, Vol. 22, No. 104, (October 1968), pp. 745-762, ISSN 0025-5718.

39. D. S. Kershaw (1978), The incomplete cholesky-conjugate gradient method for iterative solution of systems of linear equations, *J Comp Phys* (1978), Vol.26, pp. 43-65.
40. D. A. Knoll, D. B. Kothe and B. Lally (1999), A new nonlinear solution method for phase change problems, *Numerical Heat Transfer, Part B Fundamentals*, Vol. 35, No. 4, (December 1999), pp. 436–459, ISSN 1040-7790.
41. K. C. Mills (2002), *Recommended Values of Thermophysical Properties for Selected Commercial Alloys*, Woodhead Publishing Ltd, ISBN 978-1855735699, Cambridge.
42. R. Boyer, G. Welsch and E.W. Collings (1994), *Materials properties handbook: titanium alloys*, ASM International, ISBN 978-0871704818, Materials Park, OH.
43. T. Lips and B. Fritsche (2005), A comparison of commonly used re-entry analysis tools, *Acta Astronautica*, Vol. 57, No.2-8, (July-October 2005), pp. 312-323, ISSN 0094-5765

SECTION

2. CONCLUSIONS

A self-consistent three-dimensional model was developed for the laser metal deposition process by powder injection, which simulates heat transfer, phase changes, and fluid flow in the melt pool. The continuum model was adopted to deal with different phases (gas, liquid, solid, and mushy zone) in the calculation domain. The Piecewise Linear Interface Calculation (PLIC) method was implemented to track the free surface movement of the melt pool due to the powder addition and fluid flow. Surface tension was modeled by taking the Continuum Surface Force (CSF) model combined with a force-balance flow algorithm. A laser-powder interaction model was developed in this study to account for the effects of laser power attenuation and powder temperature rise during the laser metal deposition process.

Physical phenomena at the liquid/gas and solid/liquid interfaces were successfully incorporated in the governing equations as boundary conditions. The governing equations were discretized in the physical space using the finite volume method. The advection terms were approximated using the MUSCL flux limiter scheme. The fluid flow and energy equations were solved in a coupled manner. The incompressible flow equations were solved using a two-step projection method, which requires a solution of a Poisson equation for the pressure field. The discretized pressure Poisson equation was solved using the ICCG (Incomplete Cholesky Conjugate Gradient) solution technique. The energy equation was solved by an enthalpy-based method. Temperature-dependent

thermal-physical material properties were considered in the numerical implementation. The numerical model was validated by comparing simulations with experimental measurements. The model provides a means for optimizing the process parameters and controlling the process.

VITA

Zhiqiang Fan was born in the city of Zhangjiakou, China. He obtained his Bachelor's Degree in Mechanical Engineering from Harbin Engineering University in Harbin, China in 1996.

He earned his Master's Degree in Manufacturing Engineering from Missouri University of Science and Technology (Missouri S&T, formerly the University of Missouri - Rolla) in 2006. He then enrolled at the same university for his Ph. D. degree in Mechanical Engineering. He will receive his Ph. D. degree in Mechanical Engineering in May 2013.